

On the Radar Detection of Cloud Seeding Effects in Wintertime Orographic Cloud Systems

TROY J. ZAREMBA^{a,b}, ROBERT M. RAUBER^a, LARRY DI GIROLAMO^a, JESSE R. LOVERIDGE^a,
AND GREG M. MCFARQUHAR^{c,d}

^a Department of Atmospheric Sciences, University of Illinois Urbana–Champaign, Urbana, Illinois

^b Department of Atmospheric and Environmental Sciences, University at Albany, State University of New York, Albany, New York

^c Cooperative Institute for Severe and High-Impact Weather Research and Operations, University of Oklahoma, Norman, Oklahoma

^d School of Meteorology, University of Oklahoma, Norman, Oklahoma

(Manuscript received 19 September 2022, in final form 13 October 2023, accepted 16 October 2023)

ABSTRACT: Recent studies from the Seeded and Natural Orographic Wintertime Clouds: The Idaho Experiment (SNOWIE) demonstrated definitive radar evidence of seeding signatures in winter orographic clouds during three intensive operation periods (IOPs) where the background signal from natural precipitation was weak and a radar signal attributable to seeding could be identified as traceable seeding lines. Except for the three IOPs where seeding was detected, background natural snowfall was present during seeding operations and no clear seeding signatures were detected. This paper provides a quantitative analysis to assess if orographic cloud seeding effects are detectable using radar when background precipitation is present. We show that a 5-dB change in equivalent reflectivity factor Z_e is required to stand out against background natural Z_e variability. This analysis considers four radar wavelengths, a range of background ice water contents (IWC) from 0.012 to 1.214 g m⁻³, and additional IWC introduced by seeding ranging from 0.012 to 0.486 g m⁻³. The upper-limit values of seeded IWC are based on measurements of IWC from the Nevzorov probe employed on the University of Wyoming King Air aircraft during SNOWIE. This analysis implies that seeding effects will be undetectable using radar within background snowfall unless the background IWC is small, and the seeding effects are large. It therefore remains uncertain whether seeding had no effect on cloud microstructure, and therefore produced no signature on radar, or whether seeding did have an effect, but that effect was undetectable against the background reflectivity associated with naturally produced precipitation.

SIGNIFICANCE STATEMENT: Operational glaciogenic seeding programs targeting wintertime orographic clouds are funded by a range of stakeholders to increase snowpack. Glaciogenic seeding signatures have been observed by radar when natural background snowfall is weak but never when heavy background precipitation was present. This analysis quantitatively shows that seeding effects will be undetectable using radar reflectivity under conditions of background snowfall unless the background snowfall is weak, and the seeding effects are large. It therefore remains uncertain whether seeding had no effect on cloud microstructure, and therefore produced no signature on radar, or whether seeding did have an effect, but that effect was undetectable against the background reflectivity associated with naturally produced precipitation. Alternative assessment methods such as trace element analysis in snow, aircraft measurements, precipitation measurements, and modeling should be used to determine the efficacy of orographic cloud seeding when heavy background precipitation is present.

KEYWORDS: Cloud microphysics; Radars/radar observations; Weather modification

1. Introduction

The hypothesis underlying cloud seeding to enhance precipitation from wintertime orographic cloud systems is that a cloud's natural precipitation efficiency can be enhanced by converting supercooled water to ice upstream of a mountain range so that newly created ice particles can grow and fall to the surface as additional snow within a targeted area (Raubert et al. 2019; Flossmann et al. 2019). Physical evaluations of this hypothesis address four questions: 1) when and where does supercooled liquid water occur in clouds? 2) What are the natural precipitation processes, and under what conditions can the natural processes be enhanced by seeding? 3) Under what

conditions will plumes of ground- or airborne-released seeding material reach clouds upstream and within target river basins? 4) What is the microphysical chain of events following seeding that leads to additional snow that contributes to snowpack enhancement? Addressing the latter question requires in situ measurements of seeding effects with aircraft and/or with radar.

The first direct, unambiguous radar evidence of ice crystal plumes created by cloud seeding with dry ice was reported by Hobbs et al. (1981). In their experiment, dry ice was dropped from an aircraft into a nonprecipitating, broken, supercooled altocumulus cloud deck. A Ka-band (0.86 cm wavelength) vertically pointing radar located downwind of the seeding line then recorded a reflectivity plume passing over the radar that extended from the seeding level to the ground. Extensive seeding experiments were subsequently conducted over the

Corresponding author: Troy J. Zaremba, tzaremb2@illinois.edu

DOI: 10.1175/JAMC-D-22-0154.1

© 2023 American Meteorological Society. This published article is licensed under the terms of the default AMS reuse license. For information regarding reuse of this content and general copyright information, consult the AMS Copyright Policy (www.ametsoc.org/PUBSReuseLicenses).

American River basin of California during the Sierra Cooperative Pilot Project (SCPP; Reynolds and Dennis 1986). SCPP used a 5 cm wavelength scanning surveillance radar near Sheridan, California, in the Sacramento Valley. During the latter part of the SCPP between 1984 and 1986, a Ka-band vertically pointing radar was also positioned in the target area near the mountain crest in the Sierra Nevada. Seeding again was carried out with dry ice, in this case in shallow orographic clouds. Over several years, with the exception of one case, seeding signatures were not detected by either radar. In the one case, Deshler et al. (1990) reported that seeding effects were detected by the Ka-band radar in nonechoing regions of clouds in three seed lines, each line associated with radar echoes of 10–15 dBZ in otherwise nonecho regions.

Orographic cloud seeding experiments employing radars experienced over a two-decade hiatus in the United States following SCPP. The next experiment using radar, the AgI (silver iodide) Seeding Cloud Impact Investigation (ASCI; Geerts et al. 2013), occurred in 2012/13. The campaign was associated with the Wyoming Weather Modification Pilot Project (Rasmussen et al. 2018) and conducted ground-based seeding using a target/control area approach over two ranges in southern Wyoming. Pokharel et al. (2014) reported that seeding signatures were not obvious in the reflectivity patterns downwind of seeding generators in any intensive operation period (IOP) in their study. However, the composite difference (seed–no seed) of radar reflectivity for all ASCII cases in the target region in comparison with the control region showed an increase in reflectivity on both mountain ranges for each of the three radar systems employed. These included the W-band Wyoming Cloud Radar (WCR; Pazmany et al. 1994; Wang et al. 2012) on the University of Wyoming King Air (UWKA) aircraft (0.3-cm wavelength), a scanning Doppler on Wheels (DOW; Wurman et al. 2021) radar (3-cm wavelength), and a vertically pointing Micro Rain Radar (MRR, 1.2-cm wavelength).

Definitive evidence of radar seeding signatures associated with seeding in winter orographic clouds was reported in a series of recent papers (French et al. 2018; Friedrich et al. 2020, 2021) describing three IOPs from the 2017 Seeded and Natural Orographic Wintertime Clouds: The Idaho Experiment (SNOWIE; Tessendorf et al. 2019). During each of the three IOPs, light to no natural precipitation was present and seeding resulted in well-defined, traceable seeding lines. These were detected by both the airborne vertically pointing (nadir and zenith) WCR and by DOW scanning radars positioned at mountaintop locations upwind of the seeding plumes. Figure 1a, for example, shows two lines of enhanced equivalent radar reflectivity factor (Z_e) that were observed during IOP 5 at 1729:41 UTC 19 January 2017 that are the result of seeding. The University of Wyoming King Air flew repeated flight legs perpendicular to the seeding aircraft in-cloud within 1 km of cloud top at $-11^\circ < T < -14^\circ\text{C}$ to bisect the seeding signatures (Fig. 1b). Clouds in this case were dominated by supercooled liquid water (SLW), with leg-averaged, liquid water contents (LWC) ranging from 0.1 to 0.2 g m⁻³, and ice water contents (IWC) ranging between 0.01 and 0.34 g m⁻³ associated with the seeding signatures (Fig. 1c). Cloud droplet concentrations were

$< 30 \text{ cm}^{-3}$ and supercooled drizzle with diameters $> 100 \mu\text{m}$ was observed in isolated pockets, similar to natural conditions in other cases from SNOWIE (Friedrich et al. 2021, section 4a). Natural background ice particle concentrations in this case were $< 1 \text{ L}^{-1}$ and often $< 0.1 \text{ L}^{-1}$ (Friedrich et al. 2021). The only significant concentrations of ice observed at flight level were within the seeding lines and over the highest terrain more than 40 km downstream where higher Z_e was present. Background Z_e values were weak and ranged between -30 and -10 dBZ_e throughout the event and were comparable to other events where seeding signatures were observed during SNOWIE. Seeding signatures like those shown in Figs. 1a–c were not observed in any cases with high background ice concentrations.

Similar signatures in SLW clouds have been observed elsewhere. Most recently, Wang et al. (2021) used a 5.6-cm wavelength radar in central China to document a reflectivity line similar to that observed during SNOWIE. In their case, the line developed following seeding near the northern edge of a weak echo region within an orographic cloud system. A common feature of cases from the experiments discussed above is that the background signal from natural precipitation was sufficiently weak that the radar signal attributable to seeding could be clearly identified. There are no published studies of cases with heavy background precipitation where seeding effects were observed with radar.

During the 2016/17 winter season, SNOWIE carried out seeding operations during 18 IOPs. In only three was the signal on radar sufficiently clear that it could be attributed unambiguously to seeding. Except for these three cases, natural precipitation was present during seeding operations and no clear seeding signature was detected in the reflectivity field from the radars. In these IOPs, and more generally in any experiment where seeding occurs but the effects are not detected with radar against a natural background, it remains uncertain whether seeding had no effect on cloud microstructure, and therefore produced no signature on radar, or whether seeding did have an effect, but that effect was undetectable against the background reflectivity associated with naturally produced precipitation. This paper provides a quantitative analysis examining this conundrum to better understand when changes in cloud microstructure associated with seeding do or do not produce a detectable change in the radar signal against a background of natural precipitation.

2. SNOWIE and natural background variability

SNOWIE was carried out over the Payette River basin and Salmon River Mountains of western Idaho from 7 January to 16 March 2017 (Tessendorf et al. 2019). During that time 23 research flights took place, with 18 flights occurring during seeding operations. Previous work has addressed the impact of airborne seeding with silver iodide aerosol (French et al. 2018; Friedrich et al. 2020, 2021). Heimes et al. (2022, their Fig. 1) shows the location of the SNOWIE project domain along with UWKA and seeding-aircraft flight tracks. Zaremba et al. (2022, their Fig. 1) shows the SNOWIE domain in the context of the Intermountain West.

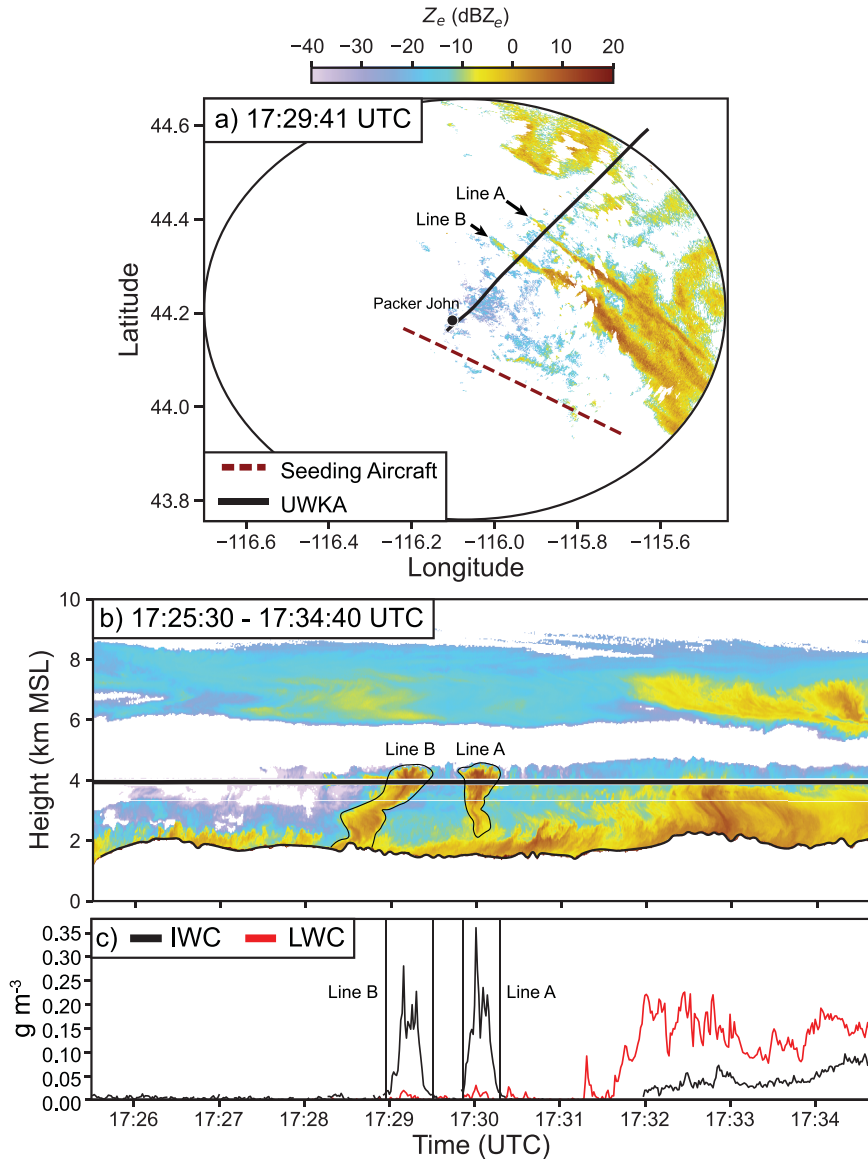


FIG. 1. (a) The Z_e from a 1° elevation scan of the X-band DOW radar on Packer John Mountain valid at 1729:41 UTC 19 Jan 2017 during IOP 5. The solid black line is the UWKA flight track. The red dashed line was the seeding-aircraft flight track. Discernable seeding lines are denoted. (b) The Z_e from the WCR between 1725:30 and 1734:40 UTC 19 Jan 2017. Seeding signatures are outlined. The black line is the UWKA flight track. (c) Nevzorov IWC (black) and LWC (red) in grams per meter cubed measured at flight level along the flight track. The black vertical lines denote signatures of IWC enhancement due to seeding.

During SNOWIE, 35 flight legs were flown prior to the onset of seeding across all IOPs. These flight legs were used to quantify the natural variability in Z_e in orographic clouds over the Payette River basin. First, linearly averaged Z_e values ($\overline{Z_e}$, then converted to $\overline{\text{dBZ}_e}$) were calculated at each altitude along each flight leg. The statistics for $\overline{Z_e}$ are shown in Fig. 2 as a contoured-frequency-by-altitude diagram (CFAD). Heights were limited to < 5 km because seeding never occurred above 4.5 km during the campaign. The median value of $\overline{Z_e}$ ranged from -5 to 0 dBZ_e throughout the cloud depth

(Fig. 2a). Figure 2a also shows that the minimum $\overline{Z_e}$ was ~ -10 dBZ_e at altitudes < 3.3 km and ranged from -35 to -10 dBZ_e above 3.3 km. The maximum $\overline{Z_e}$ ranged from 5 to 10 dBZ_e throughout the cloud depth. To quantify natural variability in Z_e along the flight legs prior to the onset of seeding, the mean of the difference in Z_e at each altitude (expressed as decibels) between the 75th and 25th and 95th and 5th quantiles of each of the 35 flight legs was calculated (Fig. 2b). The mean variability between the 25th and 75th quantiles increased from 0 dB near the surface to ~ 10 dB above 2.5 km.

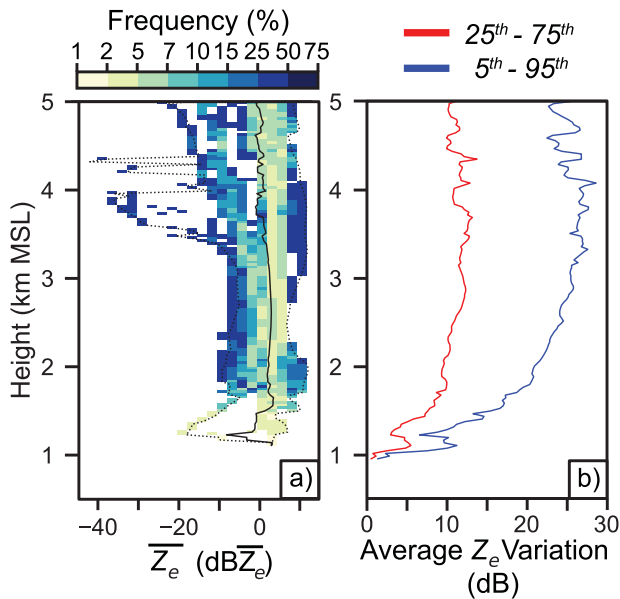


FIG. 2. Statistics of WCR Z_e along 35 flight legs during all SNOWIE IOPs prior to seeding. The seeding aircraft always seeded below 5 km. (a) CFAD of leg-averaged WCR Z_e binned every 5 dB Z_e and 100 m from the 35 legs. The solid line represents the median of the 35 leg-averaged WCR Z_e . The dotted lines represent minimum and maximum leg-averaged Z_e at a given height. (b) The average difference between the 75th and 25th percentiles of Z_e along the flight legs (red line), and the average difference between the 95th and 5th percentiles (blue line).

The mean variability between the 5th and 95th quantiles increased from 0 dB near the surface to ~ 25 dB above 3 km. Therefore, for a signal from orographic cloud seeding to stand out from the natural background variability, a seeding signature would likely have to increase Z_e by 5–10 dB or more to clearly stand out against the background. A weaker signal may be evident if it occurs in zig-zag lines downstream of the seeding-aircraft path (e.g., French et al. 2018). However, for distributed ground-based seeding, which occurs continuously, patterns such as lines would not exist. In the subsequent analysis, we examine changes in cloud IWC that would result in significant changes in Z_e (>5 –10 dB) so that the seeding signature could be observed against the natural background variability commonly observed during SNOWIE.

A Nevzorov liquid water and total water content probe (Korolev et al. 1998) provided measurements of LWC and IWC during SNOWIE. Deng et al. (2022) describes the use of the Nevzorov probe during SNOWIE. Mean IWC from the Nevzorov probe was calculated for all 238 flight legs flown during SNOWIE. Three flight legs were flown entirely outside of cloud and were not included in the statistical summary. Also, any periods during which the aircraft was out of cloud were not included in the mean for a given flight leg. Figure 3a shows that almost all flight legs flown during SNOWIE had mean IWC less than 0.30 g m^{-3} . The median value of the mean IWC for all flight legs was 0.06 g m^{-3} . Except for one flight leg the mean IWC never exceeded 0.40 g m^{-3} , although

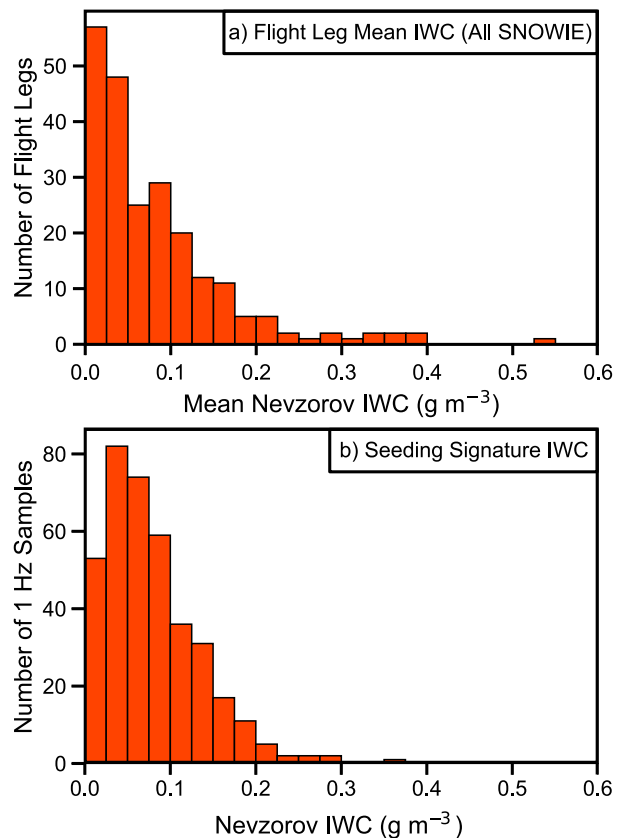


FIG. 3. (a) Flight leg-averaged Nevzorov IWC from 235 UWKA flight legs. This includes flight legs for which seeding occurred during SNOWIE. (b) One-hertz samples of Nevzorov IWC within seeding signatures. The time periods included are given in Table 1.

individual 5-Hz-averaged samples can have locally higher values (Deng et al. 2022).

The measurement of IWC by the Nevzorov probe has been investigated in wind tunnel and in situ studies. Laboratory and airborne studies employing image analysis have shown that the Nevzorov probe causes shattering of ice particles upon impact, leading to fragments that can be visibly carried away from the conical cone inlet due to airflow around the instrument (e.g., Korolev et al. 2013). Ice crystals can also bounce off the instrument and be swept away by the surrounding airflow (e.g., Strapp et al. 2005). Additionally, pools of unevaporated water from ice crystals can accumulate in the conical cone inlet, resulting in the expulsion of unevaporated water from the sensor due to nonuniform heat distribution during evaporation (Korolev et al. 2013).

Past in situ and laboratory research has determined that the IWC measured by the Nevzorov probe with a shallow cone design can be underestimated by a factor of 3.0 ± 0.2 relative to that obtained using alternative instruments (Strapp et al. 2005; Korolev et al. 2013). The UWKA Nevzorov has a deeper cone design that may lead to smaller measurement errors of IWC. However, quantitative estimates of the uncertainties in the measurement of IWC with a deeper cone

design are needed to determine the collection efficiency (Faber 2017).

3. Approach

Seeding signatures were observed to locally increase Nevzorov IWC during two SNOWIE research flights (19 January 2017 and 20 January 2017). Seeding signatures were too low to be observed in situ by the UWKA on a third flight because of strong shear but were observed by the vertically pointing WCR (Friedrich et al. 2021; 31 January 2017). Periods during which the UWKA was passing through seeding signatures are noted in Table 1. Figure 3b shows 1-Hz measurements of IWC within the observed seeding signatures. IWC typically ranged from 0.01 to 0.30 g m⁻³ within seeding signatures with a median IWC of 0.08 g m⁻³ and a 95th-percentile value of 0.18 g m⁻³. These values provide a useful range from which to explore the sensitivity of radar to changes in cloud microstructure associated with seeding. These measurements of IWC would suggest that in a heavy precipitation event where natural mean IWC approached 0.45 g m⁻³, seeding could result in a 1%–40% increase in IWC over that already in the heavily precipitating cloud.

Radiometer data and aircraft measurements show that supercooled water occurs more frequently in shallow, warmer-topped orographic clouds with low background cloud IWC (e.g., Rauber and Grant 1986; Heggli and Rauber 1988), which has led to recommendations that shallow orographic clouds with little natural background ice particle concentrations are more “seedable.” Although this is likely true in many storms, the question addressed here is not whether certain cloud systems are more seedable than others because of their cloud microstructure, but rather whether a seeding signature can be detected with radar when significant background precipitation is present. For the purposes of this study, we therefore assume the following:

- 1) SLW is available in all clouds, its concentration independent of background ice water content, and its magnitude sufficient to increase the IWC through seeding by a percentage that can range from 1% to 40% of that observed in a natural heavily precipitating cloud.
- 2) The additional ice mass created by converting SLW to ice by seeding is independent of the background IWC (i.e., a cloud with low or high values of IWC will have its IWC increased by the same amount by seeding). This is equivalent to assuming that the SLW available for conversion to ice at a given percentage level is sufficient in any cloud and independent of background IWC.
- 3) The particle size distributions (PSDs) used in this analysis are made up of spherical ice particles whose densities are based on the parameterization of Brown and Francis (1995) and indices of refraction corresponding to those for dry snow (Sadiku 1985), so that Mie scattering theory can be applied to calculate backscattered power. These assumptions will be discussed more thoroughly in sections 3b and 3d.

TABLE 1. Time periods during which seeding signatures were sampled by the UWKA. IWC from these time periods is shown in Fig. 3b.

Start time	End time	IOP
1657:53 UTC 19 Jan 2017	1658:05 UTC 19 Jan 2017	5
1718:18 UTC 19 Jan 2017	1718:51 UTC 19 Jan 2017	5
1717:32 UTC 19 Jan 2017	1717:39 UTC 19 Jan 2017	5
1729:02 UTC 19 Jan 2017	1729:26 UTC 19 Jan 2017	5
1729:51 UTC 19 Jan 2017	1730:16 UTC 19 Jan 2017	5
1740:51 UTC 19 Jan 2017	1741:14 UTC 19 Jan 2017	5
1741:43 UTC 19 Jan 2017	1742:14 UTC 19 Jan 2017	5
0048:44 UTC 20 Jan 2017	0048:49 UTC 20 Jan 2017	6
0127:44 UTC 20 Jan 2017	0129:09 UTC 20 Jan 2017	6
0126:54 UTC 20 Jan 2017	0127:00 UTC 20 Jan 2017	6
0146:02 UTC 20 Jan 2017	0147:13 UTC 20 Jan 2017	6
0148:13 UTC 20 Jan 2017	0148:38 UTC 20 Jan 2017	6
0144:46 UTC 20 Jan 2017	0145:06 UTC 20 Jan 2017	6

- 4) The radars observing the clouds use wavelengths similar to those in past airborne and ground-based studies (W band, 3 mm; Ka band, 0.86 cm; X band, 3 cm; C band, 5 cm).
- 5) The radar’s software derives the radar reflectivity factor using the standard weather radar equation obtained from Rayleigh-scattering theory (see Rauber and Nesbitt 2018).
- 6) Background ice PSDs can be represented as gamma distribution functions, where the number distribution function for a gamma distribution is given by

$$n(D) = n_o D^\mu e^{-\lambda D}, \quad (1)$$

where D is the particle diameter, n_o is the intercept parameter, λ is the slope parameter, and μ is the shape parameter.

These assumptions represent a “best case” scenario in that sufficient supercooled water will be present in heavy background precipitation. If it is not, radar detection of a seeding signature will be more difficult to ascertain. The following procedure is then used to determine whether a seeding signature can be detected with radar in the presence of background ice.

a. PSDs in heavily precipitating orographic clouds

Representative heavy background precipitation PSDs from flight legs of the UWKA during SNOWIE were constructed by merging data from two optical array probes: a two-dimensional stereo probe (2DS; Lawson et al. 2006) and a two-dimensional precipitation probe (2DP; Knollenberg 1981; Baumgardner et al. 2017). Data from the 2DS were used for particles between 100 and 1200 μm and the 2DP for particles greater than 1200 μm . The size ranges used for the 2DS and 2DP probes were determined as follows: a lower threshold (100 μm) for the 2DS was chosen to minimize uncertainty in the depth of field (e.g., Lawson et al. 2006) and to remove potentially shattered artifacts (e.g., Jackson et al. 2014). An upper threshold (1200 μm) was selected as the 2DS-2DP cutoff point where the 2DS and 2DP most consistently overlapped during SNOWIE. The 2DP array width was 6.4 mm. 2DS and 2DP data were processed using the University of Illinois/Oklahoma Optical Array Probe Processing Software

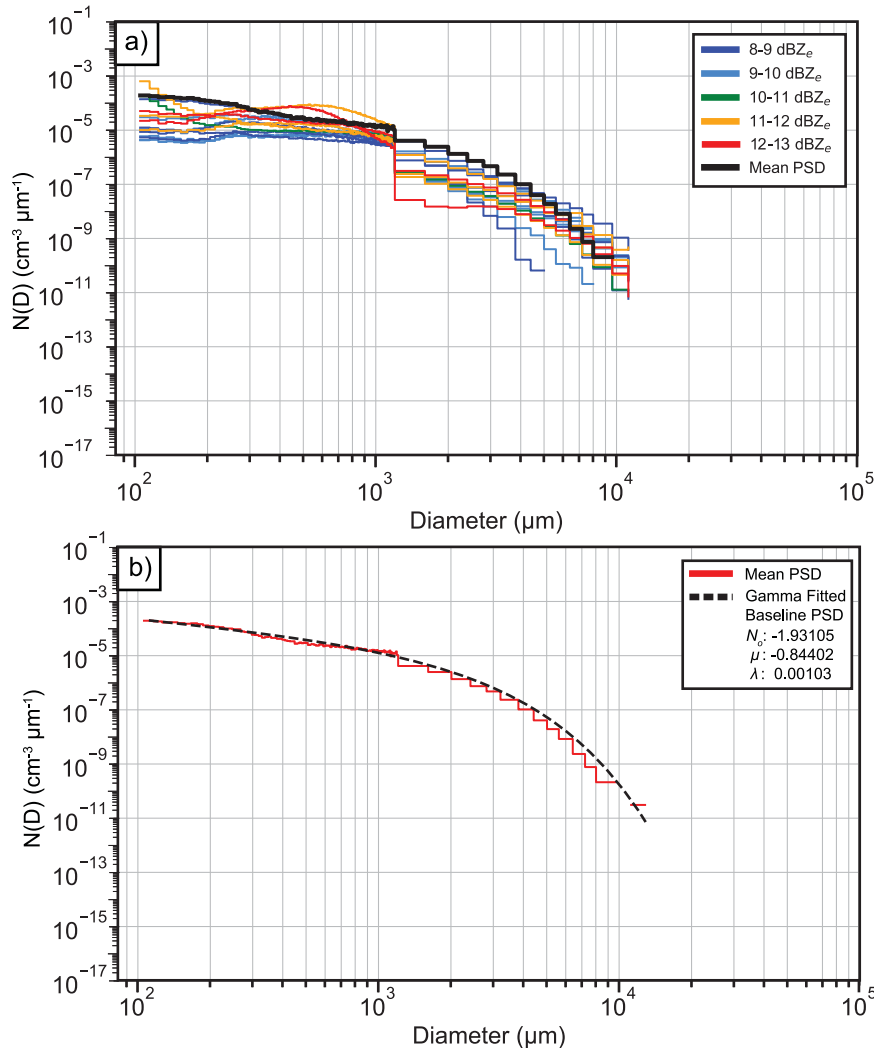


FIG. 4. (a) Mean PSD measured by the 2DS/2DP probes for all flight legs with $\overline{Z}_{e,FL} > 8$ dBZ_e. The $\overline{Z}_{e,FL}$ ranges are denoted by colors. The mean PSD used for the abbreviated time period (2240:00–2242:00 UTC 18 Jan 2017; see Fig. 6) is shown in red. (b) The gamma-fitted baseline PSD with $IWC_B = 1.214$ g m⁻³ is shown in black.

(UIOOPS; McFarquhar et al. 2018). The size of each particle was determined using the diameter of the minimum enclosing circle and PSDs were calculated at 1-Hz intervals and then averaged across the flight leg. Flight legs were typically 8–20 min long and occurred at altitudes ranging from 3.2 to 5.2 km. Flight leg lengths ranged from 19.5 to 135.6 km with a median leg length of 77.0 km. UWKA true air speeds ranged from 80.2 to 131.5 m s⁻¹ with a median true airspeed of 102 m s⁻¹. The flight legs were then sorted based on the average W-band Z_e near flight level ($\overline{Z}_{e,FL}$) along each flight leg. Flight legs with $\overline{Z}_{e,FL} > 8$ dBZ_e were isolated for further consideration.

During SNOWIE, 19 flight legs had W-band $\overline{Z}_{e,FL} > 8$ dBZ_e near the flight level. Two of these flight legs were from IOP 20 where the 2DS was not operational, and two flight legs had problems with the 2DP probe (RF02 FL7 and RF04 FL10). For the remaining 15 flight legs, mean PSDs for each flight leg were

calculated to examine the variability between the legs (Fig. 4a). These PSDs had mean volume diameters ranging from 1639 to 6657 μm, with a mean of 4515 μm. The distributions fell into two categories. In the first category, which included nine flight legs, the 2DS and 2DP showed poor agreement in their overlap region, with errors approaching two orders of magnitude (cm⁻³ μm⁻¹). This was believed to result from a problem with the 2DP probe during some SNOWIE research flights. In the second category, which included 6 flight legs, there was good agreement in their overlap region. The flight legs with smooth overlap were retained for further consideration. From these flight legs, the flight leg corresponding to the highest W-band $\overline{Z}_{e,FL}$ was chosen.

A CFAD for the flight leg was constructed from WCR data between 2233:30 and 2243:35 UTC 18 January 2017 and shows that the median W-band Z_e remained approximately constant at 10 dBZ_e between the surface and 4 km, and then decreased to

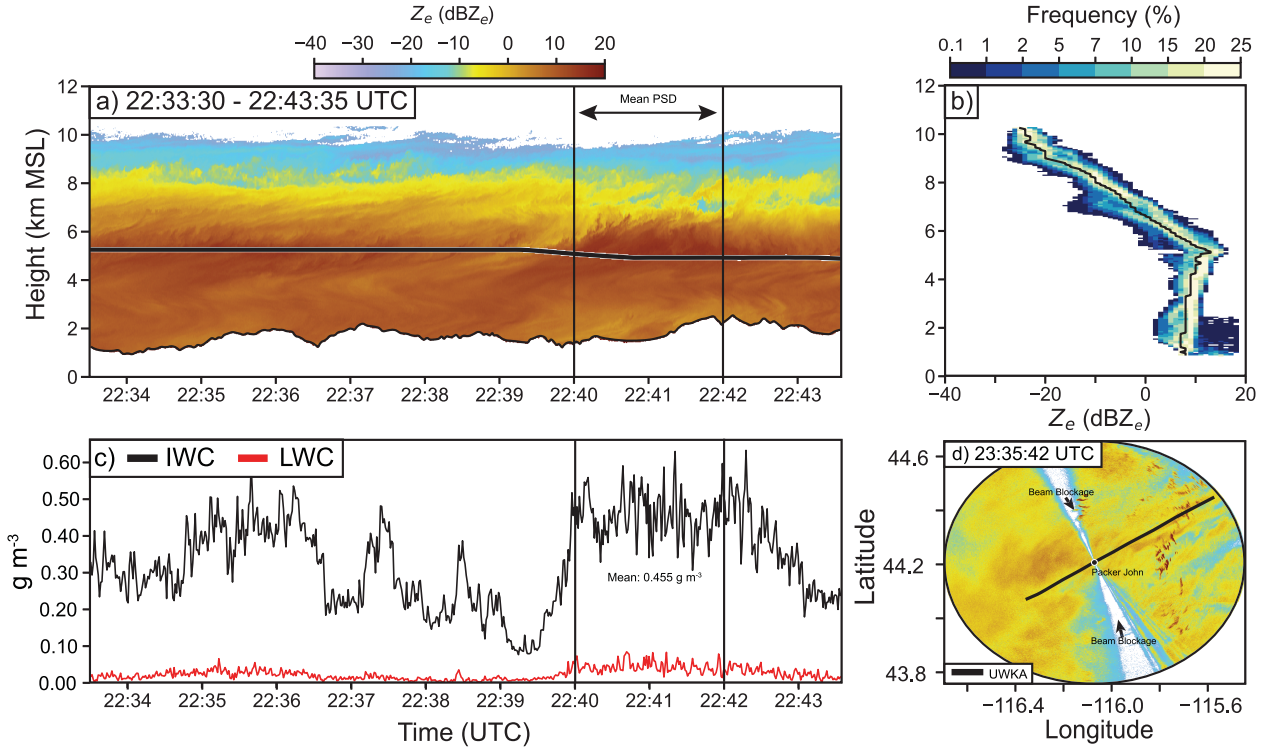


FIG. 5. (a) The Z_e from the WCR between 2233:30 and 2243:35 UTC 18 Jan 2017. The black line at 5–5.3-km altitude is the UWKA flight track; (b) CFAD of Z_e binned every 100 m in altitude and every 1 dBZ_e; (c) Nevzorov IWC (black) and LWC (red). The vertical black lines on (a) and (c) represent the time period from which the PSD in Fig. 4b was constructed. (d) The Z_e from a 1° elevation scan of the DOW radar on Packer John Mountain valid at 2335:42 UTC 18 Jan 2017. The black line is the UWKA flight track.

–20 dBZ_e near cloud echo top (Fig. 5b). The spread in Z_e values at any altitude was approximately 10 dBZ_e. The cloud system was also sampled by an X-band DOW radar, located on Packer John Mountain, a ridge upstream of the mountain range targeted by Idaho Power Company’s seeding operations (Fig. 5). The DOW 1° elevation scan in the lower part of the cloud east of Packer John showed lower values, \sim –5 dBZ_e (Fig. 5d).

A subset of the leg with the highest Z_e between 2240:00 and 2242:00 UTC 18 January 2017 was chosen to create a representative PSD in heavy precipitation, and to ensure that concentrations of the larger particles were captured. This PSD had $\overline{Z_{e,FL}} = 1.36$ dBZ_e near flight level. The mean IWC observed with the Nevzorov probe during the time period where this size distribution was averaged was 0.455 g m^{–3}. The mean volume diameter of the particle size distribution from this flight leg subset was 3277 μ m.

The ice crystal population associated with this segment, and indeed all clouds sampled during SNOWIE, had a range of habits that were poorly documented given that the best observations of habit were 2D particle images at the flight level. To correctly calculate the reflectivity from the particle size distribution would require assumptions about the habit distributions and then very complicated scattering calculations across a range of habits that in the end would have large uncertainty. The approach we took instead was to assume that the PSD is

made up of spherical particles with a consistency of dry snow, whose diameters were estimated by using the minimum enclosing diameter of the 2D images, and densities were based on the parameterization of Brown and Francis (1995).

A gamma distribution function was then fit to this natural ice particle size distribution (Fig. 4b) following McFarquhar et al. (2015) using the zeroth, second, and third moments. The IWC from the fitted gamma distribution was then calculated using

$$\text{IWC} = \sum_{i=1}^l M_i(D) n_i(D) \Delta D, \quad (2)$$

where l is the number of size bins, $n_i(D)$ is the number distribution function calculated for the i th bin, ΔD is the bin width, and $M_i(D)$ is the mass of a spherical ice particle with diameter D at the center of the i th bin. The IWC was then calculated using a variable density for ice based on Brown and Francis (1995; see their Fig. 3, solid line), which can be expressed as

$$\rho_B(D) = 140D^{-1.1}. \quad (3)$$

In this equation, ρ_B is the bulk density of an ice particle (g cm^{–3}) and D is the maximum diameter of an ice crystal (in micrometers for $D > 100$ μ m) (Atlas et al. 1995). This size distribution of spherical particles, where the density varies as a function of diameter, led to an overestimation of IWC by a factor of 2.6 relative

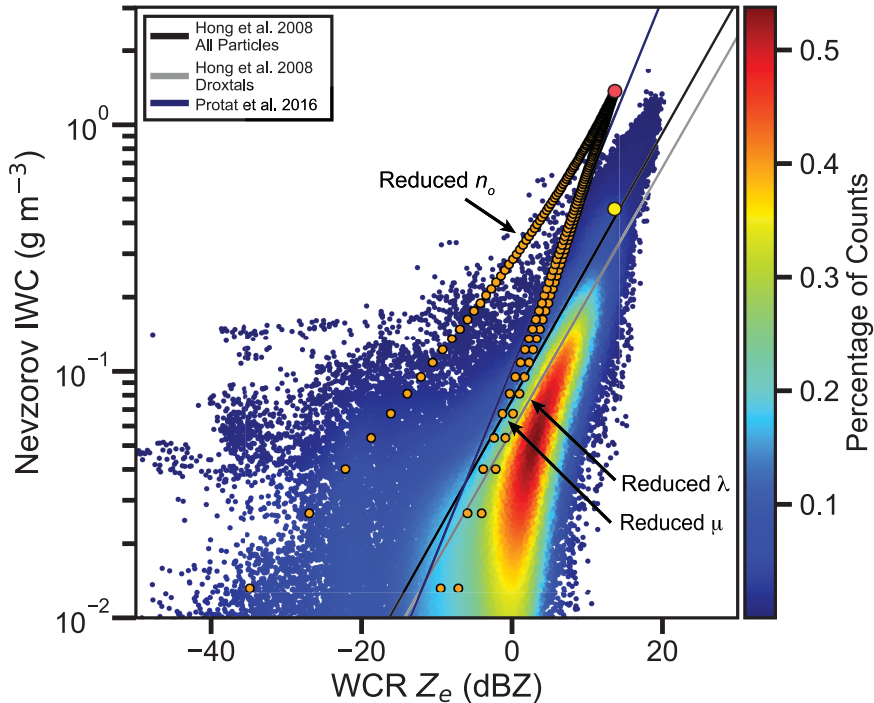


FIG. 6. A comparison of all 113 560 one-hertz Nevzorov IWC measurements during SNOWIE with WCR Z_e . Shading corresponds to percentage of overlapping data points. Lines and their respective colors correspond to different IWC/ Z_e relationships found in stratiform and winter storms. The yellow dot is the observed Z_e and IWC at flight level (13.6 dBZ and 0.455 g m^{-3}). The large orange dot corresponds to the baseline distribution (13.6 dBZ and 1.214 g m^{-3}). The small orange dots correspond to the 297 “background” PSDs that were created by reducing IWC_B systematically to $IWC = 0.99 \times IWC_B, 0.98 \times IWC_B, \dots, 0.01 \times IWC_B$ in 1% increments. The reduction was accomplished using three methods: 1) reducing n_o while holding λ and μ constant, 2) reducing μ while holding n_o and λ constant, and 3) reducing λ while holding n_o and μ constant. These are noted in the figure.

to the IWC observed by the Nevzorov probe during the heavy precipitation subset, but was within the uncertainty window of IWC underestimation by the Nevzorov probe based on past laboratory and in situ studies.

To exactly match the observed Z_e along the leg segment, the spherical particles were assumed to have an index of refraction appropriate for dry snow. The calculated real part of the index of refraction that exactly matched the measured reflectivity at W band along the leg was 1.0316, very close to the values reported by Sadiku (1985, their Table 4) for dry snow at 0°C . In the calculations that follow, we assumed that the imaginary component of the index of refraction was zero so that the ice crystals sampled did not absorb any transmitted power. This same index of refraction was also used for Mie scattering calculations for other wavelengths, based on Sadiku (1985), who reported virtually identical indices of refraction for the wavelengths used in this paper. The final gamma distribution was

$$n(D) = -1.93105D^{-0.84402}e^{-0.00103D}, \quad (4)$$

and will herein be referred to as the “baseline cloud IWC,” $IWC_B = 1.214 \text{ g m}^{-3}$, and will remain fixed throughout the remainder of this paper (Fig. 7 below; blue box).

Figure 6 shows the position of the baseline distribution in IWC/ Z_e space relative to all simultaneous 113 560 one-hertz measurements of IWC/ Z_e by the Nevzorov probe and the WCR. Z_e values from the aircraft were determined by interpolating between the first valid range gates above and below the aircraft flight level to the level of the aircraft. Most aircraft measurements fell beneath IWC/ Z_e relationships reported in Hong et al. (2008), which used data from several field campaigns to build IWC/ Z_e relationships for all observed ice crystals and droxtals and Protat et al. (2016) who analyzed stratiform clouds over the tropics. The position of the baseline distribution point is slightly above the cloud of points in Fig. 6. However, if the Nevzorov IWC is an underestimate of the true IWC, the cloud of data for a true measure of IWC would move upward on the figure. In this case, the baseline distribution would be near the peak of the cloud of data and would therefore represent a very heavily precipitating background ice cloud.

b. Background cloud PSDs with reduced IWC

To create PSDs for “background” clouds with reduced IWC, the IWC was then systematically reduced from IWC_B by

modifying the baseline gamma distribution. The goal was to determine the reduction in IWC needed to detect a seeding effect with radar that exceeds background variability. Additional “background” PSDs were created by reducing IWC_B systematically to $IWC = 0.99 \times IWC_B$, $0.98 \times IWC_B$, etc., to $0.01 \times IWC_B$ in 1% increments. The reduction was accomplished using three methods: 1) reducing n_o while holding λ and μ constant, 2) reducing μ while holding n_o and λ constant, and 3) reducing λ while holding n_o and μ constant. In this manner, 297 additional ice particle size distributions were created. The reason for reducing n_o , μ , and λ in this manner is to create background cloud ice particle size distributions with lower IWC by systematically reducing the number of particles in IWC_B . The goal is to simulate lighter precipitation events to determine when seeding would be detectable using radar.

The justification for testing each of the three parameters (n_o , λ , and μ) independently is that microphysical processes can have effects on any or all of the three parameters of the gamma distribution. For example, accretion of cloud drops (riming) will not change n_o but can change μ or λ because the collection efficiencies of ice particles for water droplets vary as a function of particle size and habit. Aggregation of particles has an effect on n_o but also changes μ and λ . The rate of ice particle growth by diffusion is a function of particle diameter. Although this will not affect n_o , it will likely have an effect on μ or λ . Sublimation effectively reduces the small particles relative to the large particles, changing n_o , μ , and λ .

Results discussed herein are for 75%, 50%, 25%, 10%, 5%, and 1% reductions of IWC_B [Fig. 7 (green boxes); Fig. 8]. Reducing n_o had the effect of reducing the concentration in each size bin by the same amount regardless of size, effectively translating the distribution to lower concentrations, resulting in a reduction relative to IWC_B (Fig. 8a). Reducing μ resulted in a larger fractional reduction in large particles relative to small particles (Fig. 8b). Reducing λ changed the slope of the distribution, resulting in a larger reduction in the concentration of largest particles relative to the smaller particles (Fig. 8c).

c. Seeded distributions

Seeding was simulated by adjusting the baseline size distribution to increase the IWC systematically to $1.01 \times IWC_B$ through $1.40 \times IWC_B$ in varying increments (1%, 5%, 10%, 15%, 20%, 30%, and 40%), again using three methods: 1) increasing n_o while holding λ and μ constant, 2) increasing μ while holding n_o and λ constant, and 3) increasing λ while holding n_o and μ constant (Fig. 9). Increasing n_o , μ , and λ in this manner again had the primary effect of systematically increasing different parts of the baseline size distribution, respectively. These 45 “seeded” size distributions are noted on Fig. 7 (yellow box).

For clouds with reduced background IWC (e.g., those in the green boxes in Fig. 7), regardless of the IWC of the background cloud, the increment in IWC due to seeding was a Δ of IWC_B . In other words, the amount of new ice introduced into the cloud was independent of the background IWC but was a fractionally greater amount for instances with lower background IWC. The resulting IWC for these clouds are shown on Fig. 7 (pink boxes). Figures 10–12 show the modifications to

the background cloud particle size distributions as a result of seeding for three values of background IWC, 50%, 10% and 1%, of IWC_B .

d. Calculated change in reflectivity resulting from seeding

There is substantial variability in the backscattering efficiency of ice particles when the index of refraction is taken as a function of ice density, which itself depends on other factors, such as ice crystal habit and temperature. Habits are variable and unknown when collecting radar observations. In this study, spherical particles were chosen for the ease of employing Mie scattering theory. We follow the procedure used by Eriksson et al. (2018) and the database they created for the single scattering properties at microwave frequencies. This is a widely used and comprehensive database of single scattering properties for a wide range of ice habits, including the spheres we have used here. Based on figures in Eriksson et al. (2018), we can appreciate that there exist orders of magnitude differences in backscattering efficiencies at certain frequencies and size parameters across ice crystal habits. When taking ratios of backscattering efficiency between populations sizes [see Eq. (13)], the variability across habit is mitigated for frequencies and sizes used in this study based on figures in Eriksson et al. (2018), but not completely removed. Therefore, the use of spherical snow particles with an index of refraction consistent with dry snow (Sadiku 1985) is a limiting assumption, as would be the use of any other assumed habit. As will be discussed below, we are not focused on the backscattered power from a particular baseline PSD, but rather the ratio of backscattered power between seeded and unseeded PSDs.

For a given size distribution function $n(D)$ of spherical snow particles, the volume scattering coefficient β_s for the distribution is

$$\beta_s = \int_0^\infty n(D)Q_s(D)\frac{\pi}{4}D^2 dD, \quad (5)$$

where $Q_s(D)$ is the scattering efficiency factor. The scattering phase function p is the scattering cross-section weighted average of the phase function:

$$p(\cos\Theta) = \frac{1}{\beta_s} \int_0^\infty n(D)Q_s(D)\frac{\pi}{4}D^2 p(\cos\Theta; D) dD, \quad (6)$$

where Θ is the scattering angle. For radar backscatter, $\cos\Theta = -1$. In general, the backscattered power P received by the radar antenna illuminating a volume of spherical snow particles at distance R from the radar is equal to

$$P = C_1\beta_s p(-1), \quad (7)$$

where the value of C_1 depends on R and the characteristics of the radar employed and the scattering phase function is evaluated in the backscatter direction, where propagation effects are neglected.

For a given size distribution $n(D)_0$, the backscattered power received by the radar antenna is equivalent to

$$P[n(D)_0] = C_1\beta_{s_0}p_0(-1). \quad (8)$$

Background ice particle distribution IWC ($g\ m^{-3}$)

Seeded ice particle distribution IWC ($g\ m^{-3}$)

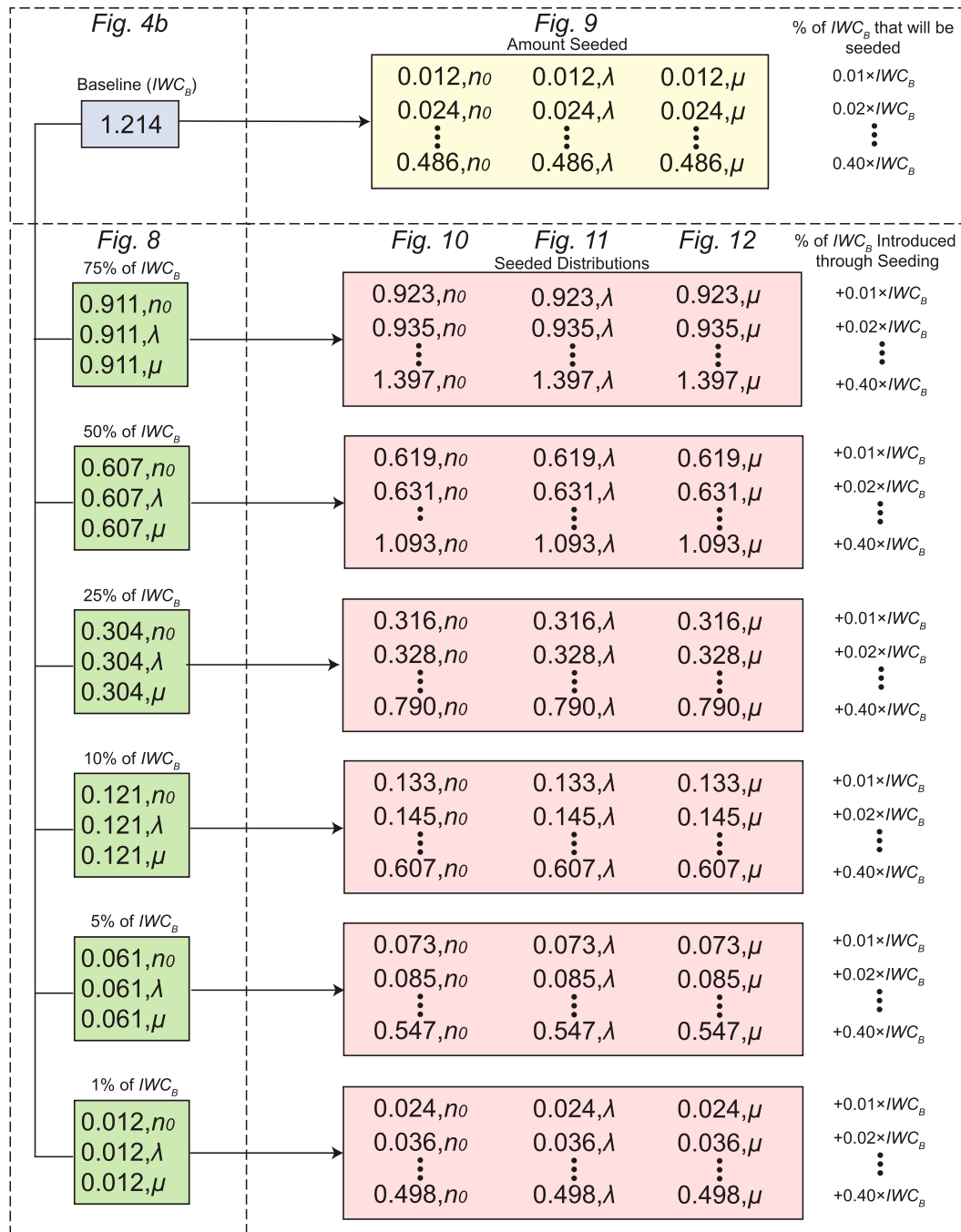


FIG. 7. The blue box is the baseline ice water content IWC_B . The green boxes denote (IWC, p) , where IWC is the reduced background IWC created to simulate weaker background precipitation events and p is the parameter ($no, \lambda, \text{ or } \mu$) changed to achieve the reduction (see Fig. 8). The yellow boxes denote (IWC, p) , where IWC is the increase in IWC as a result of seeding and p is the parameter ($no, \lambda, \text{ or } \mu$) changed to achieve the increase. The pink boxes show (IWC, p) , where IWC is the total IWC (background plus seeded) after seeding and p is the parameter ($no, \lambda, \text{ or } \mu$) changed for both the reduction (background IWC) and the additional IWC associated with seeding.

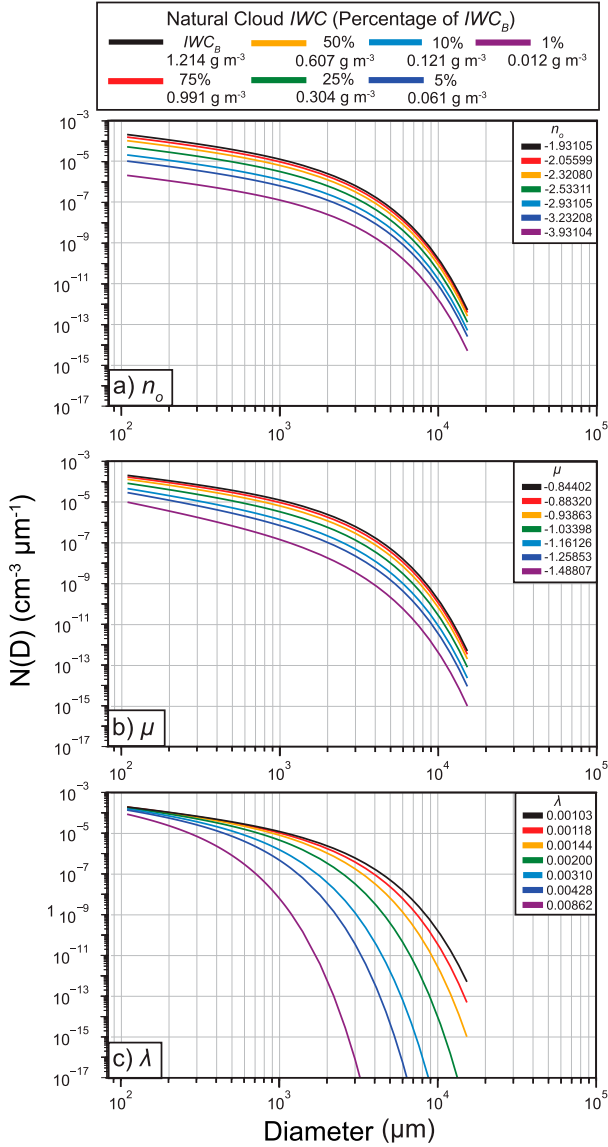


FIG. 8. Modified background PSDs (corresponding to the green boxes in Fig. 7) with IWC that is a percentage of IWC_B . The PSDs were obtained by (a) modifying n_o while holding μ and λ constant, (b) modifying μ while holding n_o and λ constant, and (c) modifying λ while holding n_o and μ constant.

For a new size distribution $n(D)_x$, where we will use x to represent the percent increase in IWC of the size distribution due to seeding, the backscattered power received by the radar antenna is equivalent to

$$P[n(D)_x] = C_1 \beta_s p_x(-1). \quad (9)$$

Radar processing software used in research and operations calculates the reflectivity in terms of Rayleigh scatterers composed of liquid water. The radar equation for Rayleigh scattering for a radar illuminating a distributed target of spherical snow particles with a given size distribution $n(D)_0$, at distance R is given by

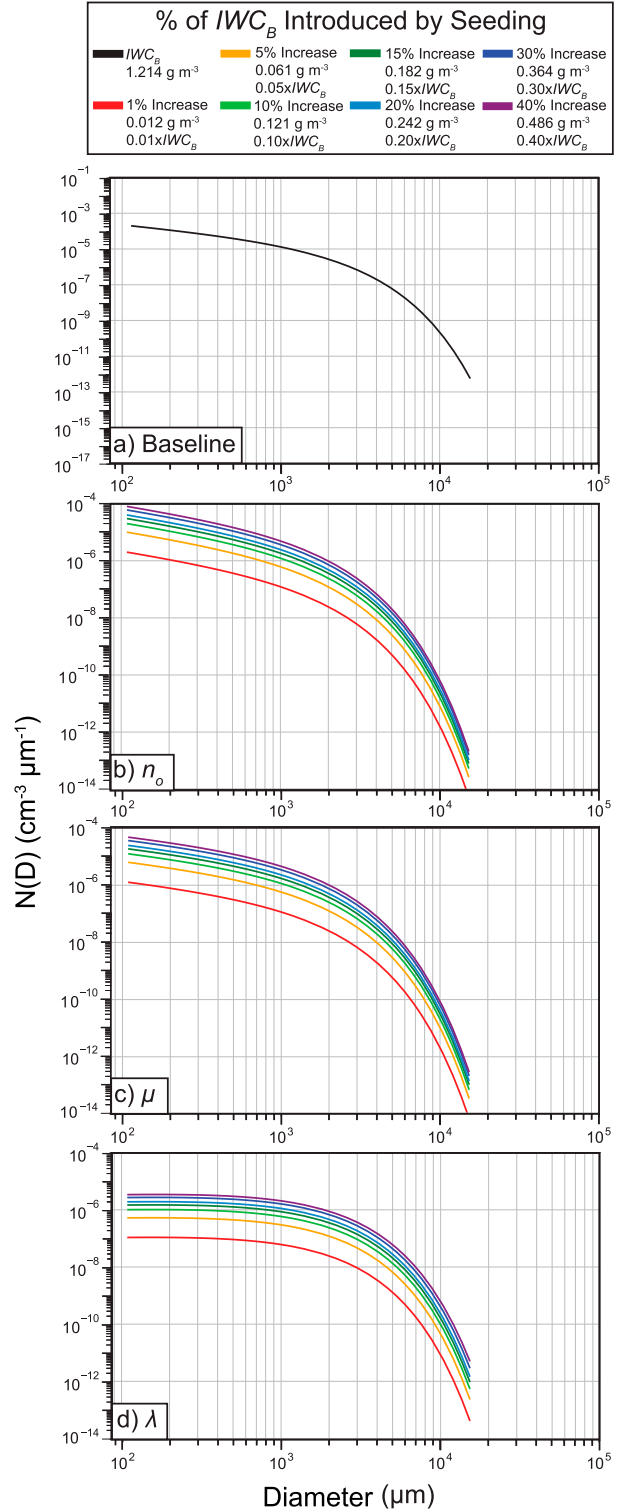


FIG. 9. (a) Baseline size distribution (blue box in Fig. 7) and (b)–(d) incremental increase in particle concentrations due to seeding to be added to IWC_B (yellow box in Fig. 7). The seeding increments to the IWC_B PSDs were obtained by modifying n_o while holding μ and λ constant [in (b)], modifying μ while holding n_o and λ constant [in (c)], and modifying λ while holding n_o and μ constant [in (d)].

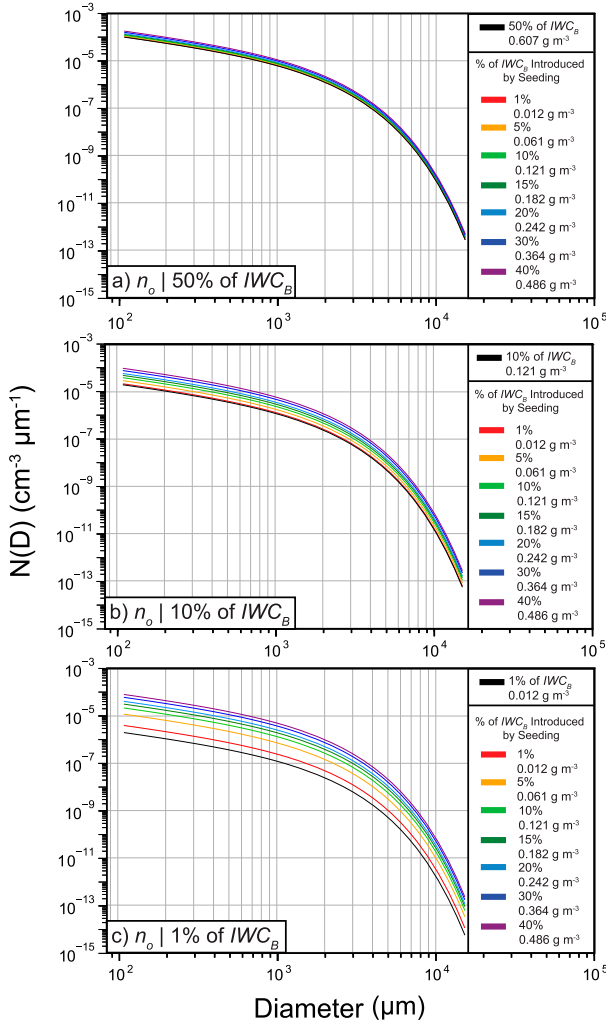


FIG. 10. Change in PSDs as a result of seeding three background PSDs having $IWC = (a) 0.50 \times IWC_B$, $(b) 0.10 \times IWC_B$, and $(c) 0.01 \times IWC_B$. The seeded PSDs were created by modifying n_o while holding μ and λ constant.

$$P[n(D)_0] = C_2 Z[n(D)_0], \quad (10)$$

where C_2 depends on R and radar characteristics and the complex index of refraction for liquid water, where Z is the sixth moment of the size distribution and is called the radar reflectivity factor. For a given size distribution $n(D)_x$, where x represents the percent increase in IWC of the size distribution due to seeding, the radar equation for Rayleigh scattering is given by

$$P[n(D)_x] = C_2 Z[n(D)_x]. \quad (11)$$

For Mie scattering, the ratio of the power received from a volume of particles with a size distribution $n(D)_x$, IWC_x , and an index of refraction of dry snow, to that of the original background size distribution $n(D)_0$ will therefore result in a change in the observed equivalent reflectivity factor of

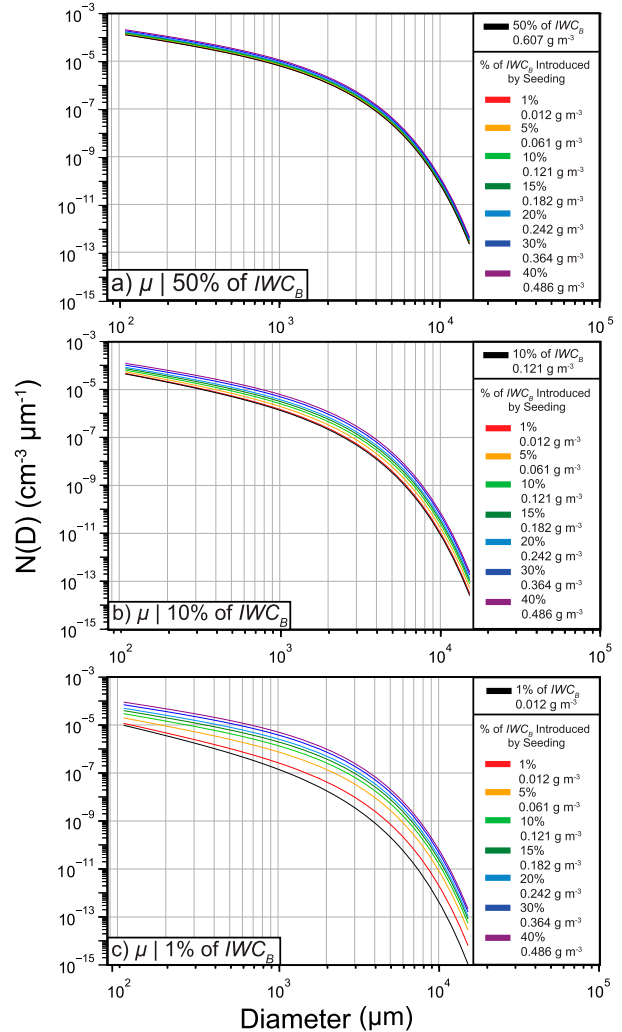


FIG. 11. As in Fig. 10, but the seeded PSDs were created by modifying μ while holding n_o and λ constant.

$$\frac{P[n(D)_x]}{P[n(D)_0]} = \frac{\beta_{s_x} p_x(-1)}{\beta_{s_0} p_0(-1)} = \frac{Z[n(D)_x]}{Z[n(D)_0]}. \quad (12)$$

From this, the change in equivalent reflectivity factor in logarithmic units as a result of seeding can be obtained:

$$\Delta dB = dB_{n(D)_x} - dB_{n(D)_0} = 10 \log_{10} \frac{\beta_{s_x} p_x(-1)}{\beta_{s_0} p_0(-1)}. \quad (13)$$

To calculate the volume backscatter coefficient $[\beta_s p(-1)]$ of the particle size distributions we assume that all particles are spherical dry snow (Sadiku 1985). We neglect the contribution to the volume backscatter coefficient from supercooled cloud droplets, which are small and scatter weakly in the microwave. The volume backscatter coefficient of individual particles was computed using Mie scattering calculations from the code distributed with the Spherical Harmonic Discrete Ordinate Method for 3D Atmospheric Radiative Transfer

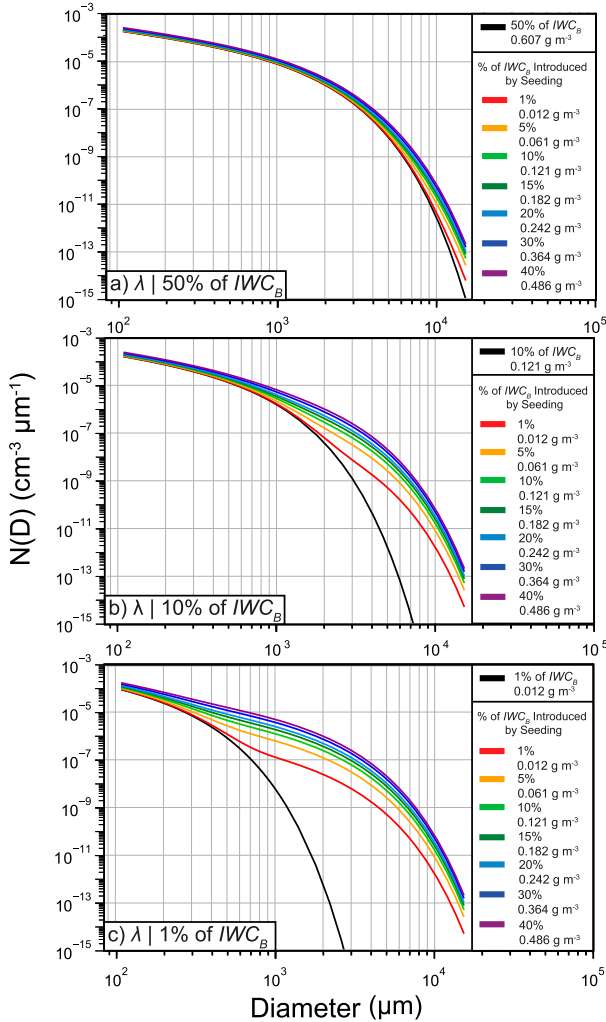


FIG. 12. As in Fig. 10, but the seeded PSDs were created by modifying λ while holding n_o and μ constant.

(SHDOM; Evans 1998). The index of refraction of four radar wavelengths (W, Ka, X, and C band) was calculated by choosing the real component of the index of refraction that allowed us to retrieve the observed W-band reflectivity while also preserving the original size distribution as discussed in section 3a. The real part of the index of refraction used in this analysis was 1.0316. This was near the reported real index of refraction for dry snow at 0°C at microwave frequencies (1.016; Sadiku 1985). Integration of the backscatter coefficient over the particle size distribution was performed to obtain the backscatter coefficient for the distribution of particles.

4. Results

As noted above, the IWC_B was reduced as a percentage by modifying n_o , μ , and λ to create modified background size distributions with lower IWCs to simulate lighter precipitation events. These reduced size distributions then had their IWC increased by a percent of IWC_B , where the percent ranged

from 1% to 40%, independent of the background IWC. This was done to determine when seeding would be detectable using radar. The 1%–40% increase in IWC is based on Nevzorov-measured IWC within seeding signatures, as discussed in section 3. Figure 13 shows the change in Z_e due to seeding as a function of the percentage of IWC_B for four radar wavelengths (W, Ka, X, and C) and seeding impacts of 1%, 5%, 10%, 15%, 20%, 30%, and 40%.

a. Changes in Z_e as a result of seeding by modifying the intercept parameter n_o

Simulating seeding by changing n_o increased the concentration of particles in all size bins in the PSD by the same amount regardless of size. Figure 9b shows the additional ice particles added to the distribution to simulate seeding that result in a percentage increase in IWC_B . Figure 10 shows how distributions that have 0.5, 0.1, and 0.01 IWC_B (0.607, 0.121, and 0.012 g m^{-3}) were modified as a result of seeding with 1%–40% increases in IWC_B (from +0.012 to +0.486 g m^{-3}) independent of the original background.

Figures 13a–d and Table 2 summarize the effects of seeding by modifying n_o . Table 2 columns 1 and 2 show the IWC (and the percentage of IWC_B) added as a result of seeding to a background IWC (columns 3–9) needed to produce a 1-, 2-, 3-, 5-, 10-, 15-, and 20-dB increase in Z_e above background. Total IWC in a seeded volume on Table 2 is the sum of the IWC introduced by seeding (column 2) and that of the background cloud (columns 3–9). For example, looking at the bold-face values on Table 2 at W band, if 1% of IWC_B (0.012 g m^{-3}) was added to a cloud by seeding, a radar observation of that cloud, if it originally had background IWC equal to 3% of IWC_B (0.036 g m^{-3}), would result in a 1-dB increase in Z_e . The total IWC after seeding in this case would be the sum of the cells in columns 2 and 3, which is 0.048 g m^{-3} .

From Table 2, for all wavelengths, an increase of 5 dB above background cannot be achieved by seeding unless background IWC is less than $0.18 IWC_B$ (0.219 g m^{-3}) and the seeding effect large (40% IWC_B). The background IWC would have to be even lower for a smaller seeding effect to produce a 5-dB difference in Z_e . For example, to achieve a change in Z_e of 5 dB above background, the background IWC would have to be less than $0.02 IWC_B$ (0.024 g m^{-3}) with a 5% seeding effect (+0.061 g m^{-3}), less than $0.06 IWC_B$ (0.073 g m^{-3}) with a 15% seeding effect (+0.182 g m^{-3}), and less than $0.18 IWC_B$ (0.219 g m^{-3}) with a 40% seeding effect (+0.486 g m^{-3}). A background IWC less than $0.04 IWC_B$ (0.049 g m^{-3}) is required for a 10-dB increase above background for all radar wavelengths given a 40% seeding effect (+0.486 g m^{-3}) and less than $0.01 IWC_B$ (0.012 g m^{-3}) with a 10% seeding effect (+0.121 g m^{-3}). To get a 15-dB seeding effect, the background IWC would have to be less than $0.01 IWC_B$ (0.012 g m^{-3}) given a 40% seeding effect (+0.486 g m^{-3}). In short, adding the same concentration to all particle size bins to the background concentration in those size bins by modifying n_o would only produce a detectable signal if background IWC was small and the seeding effect was large. Table 2 shows similar results for other wavelengths.

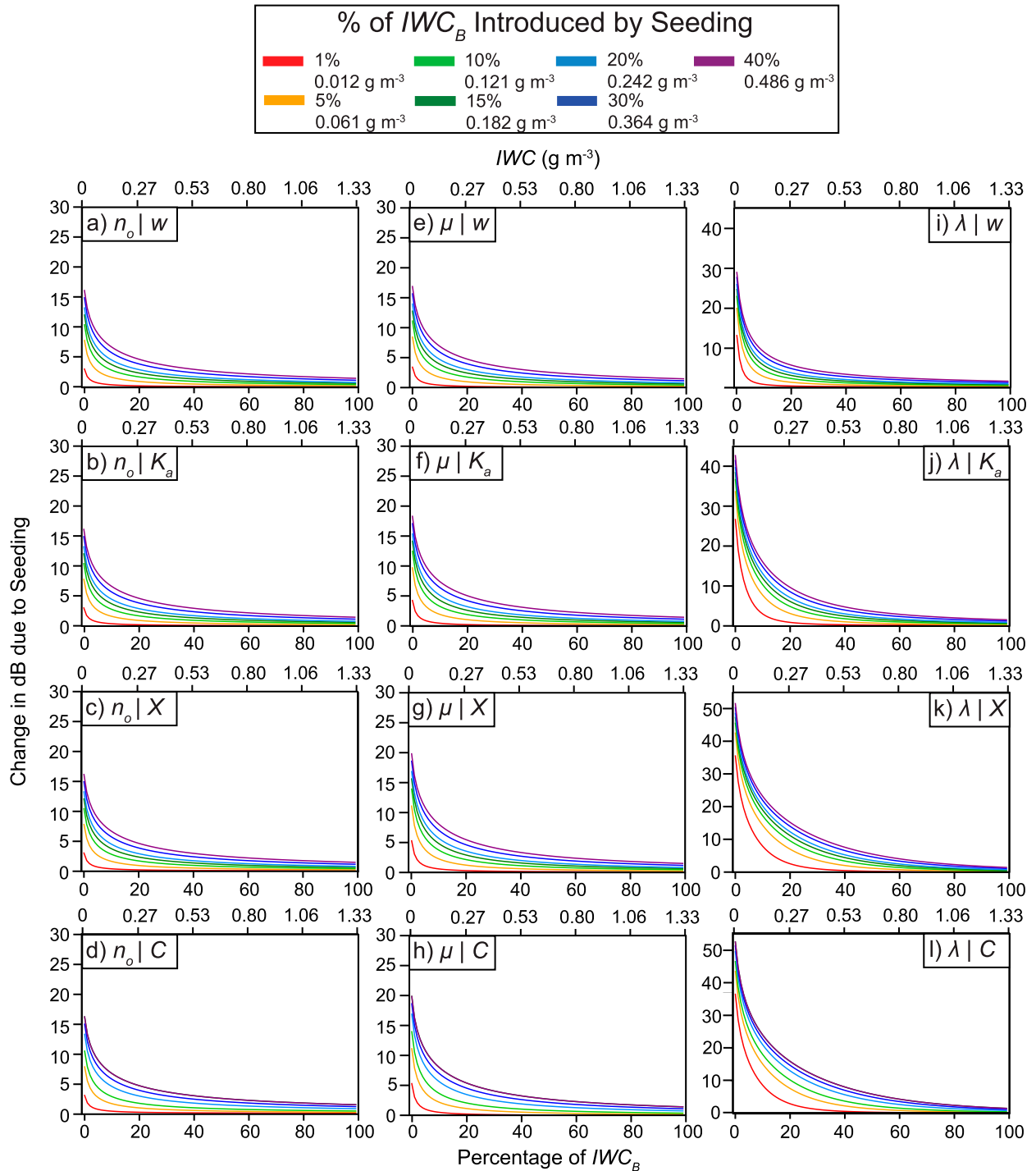


FIG. 13. Change in observed Z_e (dB) as a result of seeding as a function of background IWC for W-, Ka-, X-, and C-band radars. The bottom x axis for each panel is the percent of IWC_B , and the top axis is the actual background IWC. The y axis is the change in Z_e due to seeding. Different color lines represent the different values of IWC added to the background distributions as a result of seeding.

b. Changes in Z_e as a result of seeding by modifying the shape parameter μ

Simulating seeding by changing the shape parameter μ increased all size bins in the PSD, but there was a larger

fractional increase in large particles relative to small particles. Figure 9c shows the additional ice particles added to the distribution to simulate seeding to produce a percentage increase in IWC_B . Figure 11 shows how distributions that have 0.5, 0.1,

TABLE 2. Columns 3–9 represent the minimum background IWC [expressed as IWC (g m^{-3}) and (following the comma) a percentage of IWC_B] required to achieve a specified 1–20-dB increase in reflectivity (ΔZ_e), after varying amounts of IWC are introduced through seeding (as specified in columns 1–2). The total IWC is the sum of the IWC (second column) introduced by seeding for +1%–40% of IWC_B , as indicated in the first column, and the background IWC (columns 3–9). The boldface data are used in the text as an explanatory example of this calculation. Data in the table correspond to Figs. 13a–d. Background IWC was reduced by modifying n_o .

% of IWC_B introduced by seeding	IWC introduced by seeding (g m^{-3})	Background IWC (g m^{-3}), % of IWC_B (for different ΔZ_e)						
		1 dB	2 dB	3 dB	5 dB	10 dB	15 dB	20 dB
W band								
1%	0.012	0.036, 3	0.012, 1	0.012, 1				
5%	0.061	0.231, 19	0.097, 8	0.061, 5	0.024, 2			
10%	0.121	0.461, 38	0.206, 17	0.121, 10	0.049, 4	0.012, 1		
15%	0.182	0.692, 57	0.304, 25	0.182, 15	0.073, 6	0.012, 1		
20%	0.243	0.935, 77	0.413, 34	0.243, 20	0.109, 9	0.024, 2		
30%	0.364	1.214, 100	0.619, 51	0.364, 30	0.158, 13	0.036, 3		
40%	0.486	1.214, 100	0.826, 68	0.486, 40	0.219, 18	0.049, 4	0.012, 1	
Ka band								
1%	0.012	0.036, 3	0.012, 1	0.012, 1				
5%	0.061	0.231, 19	0.097, 8	0.061, 5	0.024, 2			
10%	0.121	0.461, 38	0.206, 17	0.121, 10	0.049, 4	0.012, 1		
15%	0.182	0.692, 57	0.304, 25	0.182, 15	0.073, 6	0.012, 1		
20%	0.243	0.935, 77	0.413, 34	0.243, 20	0.109, 9	0.024, 2		
30%	0.364	1.214, 100	0.619, 51	0.364, 30	0.158, 13	0.036, 3		
40%	0.486	1.214, 100	0.826, 68	0.486, 40	0.219, 18	0.049, 4	0.012, 1	
X band								
1%	0.012	0.036, 3	0.012, 1	0.012, 1				
5%	0.061	0.231, 19	0.097, 8	0.061, 5	0.024, 2			
10%	0.121	0.461, 38	0.206, 17	0.121, 10	0.049, 4	0.012, 1		
15%	0.182	0.692, 57	0.304, 25	0.182, 15	0.073, 6	0.012, 1		
20%	0.243	0.935, 77	0.413, 34	0.243, 20	0.109, 9	0.024, 2		
30%	0.364	1.214, 100	0.619, 51	0.364, 30	0.158, 13	0.036, 3		
40%	0.486	1.214, 100	0.826, 68	0.486, 40	0.219, 18	0.049, 4	0.012, 1	
C band								
1%	0.012	0.036, 3	0.012, 1	0.012, 1				
5%	0.061	0.231, 19	0.097, 8	0.061, 5	0.024, 2			
10%	0.121	0.461, 38	0.206, 17	0.121, 10	0.049, 4	0.012, 1		
15%	0.182	0.692, 57	0.304, 25	0.182, 15	0.073, 6	0.012, 1		
20%	0.243	0.935, 77	0.413, 34	0.243, 20	0.109, 9	0.024, 2		
30%	0.364	1.214, 100	0.619, 51	0.364, 30	0.158, 13	0.036, 3		
40%	0.486	1.214, 100	0.826, 68	0.486, 40	0.219, 18	0.049, 4	0.012, 1	

and 0.01 IWC_B (0.607, 0.121, and 0.012 g m^{-3}) were modified as a result of seeding by adding 1%–40% increases in IWC_B (from +0.012 to +0.486 g m^{-3}) independent of the original background IWC.

Figures 13e–h and Table 3 summarize the effects of seeding by modifying μ . From Table 3, for W- and Ka-band wavelengths, an increase of 5 dB above background cannot be achieved by seeding if seeding produced an increase in IWC_B less than 5% (0.061 g m^{-3}). To achieve a change in Z_e of 5 dB above background, the background IWC would have to be less than 0.02 IWC_B (0.024 g m^{-3}) with a 5% seeding effect (+0.061 g m^{-3}), less than 0.07 IWC_B (0.085 g m^{-3}) with a 15% seeding effect (+0.182 g m^{-3}) and less than 0.31 IWC_B (0.255 g m^{-3}) with a 40% seeding effect (+0.486 g m^{-3}) at W band. Wavelength differences appeared when μ was used to modify the distributions. A background IWC of 0.01 IWC_B (0.012 g m^{-3}) would result in a 15-dB increase above background

for a 20%–30% (+0.243–0.486 g m^{-3}) seeding effect for a W- and Ka-band radar, and a 15%–20% (+0.182–0.243 g m^{-3}) seeding effect for a X- or C-band radar. Again, adding medium-sized particles to the background particle size distributions by modifying μ produced a limited increase in Z_e as a result of seeding, requiring a weak background IWC for a seeding effect to be discernable at any radar wavelength, given the natural variability of Z_e within orographic clouds (Fig. 2b).

c. Changes in Z_e as a result of seeding by modifying the slope parameter λ

Simulating seeding by changing the slope parameter λ has the primary effect of adding large particles to the size distribution. Figure 9d shows the additional ice particles added to the distribution to simulate seeding to produce a percentage increase in IWC_B . Figure 12 shows how distributions that have 0.5, 0.1, and 0.01 IWC_B (0.607, 0.121, and 0.012 g m^{-3}) were

TABLE 3. As in Table 2, but background IWC was reduced by modifying μ .

% of IWC _B introduced by seeding	IWC introduced by seeding (g m ⁻³)	Background IWC (g m ⁻³), % of IWC _B (for different ΔZ_e)						
		1 dB	2 dB	3 dB	5 dB	10 dB	15 dB	20 dB
W band								
1%	0.012	0.049, 4	0.012, 1	0.012, 1				
5%	0.061	0.243, 20	0.109, 9	0.061, 5	0.024, 2			
10%	0.121	0.473, 39	0.206, 17	0.121, 10	0.061, 5	0.012, 1		
15%	0.182	0.704, 58	0.316, 26	0.182, 15	0.085, 7	0.012, 1		
20%	0.243	0.947, 78	0.449, 37	0.279, 23	0.134, 11	0.036, 3	0.012, 1	
30%	0.364	1.214, 100	0.656, 54	0.401, 33	0.194, 16	0.049, 4	0.012, 1	
40%	0.486	1.214, 100	0.850, 70	0.522, 43	0.255, 31	0.061, 5	0.012, 1	
Ka band								
1%	0.012	0.061, 5	0.024, 2	0.012, 1				
5%	0.061	0.267, 22	0.121, 10	0.073, 6	0.036, 3			
10%	0.121	0.498, 41	0.231, 19	0.146, 12	0.073, 6	0.012, 1		
15%	0.182	0.728, 60	0.340, 28	0.206, 17	0.097, 8	0.024, 2		
20%	0.243	0.947, 78	0.449, 37	0.279, 23	0.134, 11	0.036, 3	0.012, 1	
30%	0.364	1.214, 100	0.656, 54	0.401, 33	0.194, 16	0.049, 4	0.012, 1	
40%	0.486	1.214, 100	0.85, 70	0.522, 43	0.255, 31	0.061, 5	0.012, 1	
X band								
1%	0.012	0.073, 6	0.036, 3	0.024, 2	0.012, 1			
5%	0.061	0.291, 24	0.146, 12	0.085, 7	0.049, 4	0.012, 1		
10%	0.121	0.534, 44	0.267, 22	0.170, 14	0.085, 7	0.024, 2		
15%	0.182	0.753, 62	0.376, 31	0.231, 19	0.121, 10	0.036, 3	0.012, 1	
20%	0.243	0.971, 80	0.473, 39	0.304, 25	0.158, 13	0.036, 3	0.012, 1	
30%	0.364	1.214, 100	0.680, 56	0.425, 35	0.219, 18	0.061, 5	0.012, 1	
40%	0.486	1.214, 100	0.874, 72	0.546, 45	0.279, 23	0.085, 7	0.024, 2	
C band								
1%	0.012	0.073, 6	0.036, 3	0.024, 2	0.012, 1			
5%	0.061	0.291, 24	0.146, 12	0.085, 7	0.049, 4	0.012, 1		
10%	0.121	0.534, 44	0.267, 22	0.170, 14	0.085, 7	0.024, 2		
15%	0.182	0.753, 62	0.376, 31	0.231, 19	0.121, 10	0.036, 3	0.012, 1	
20%	0.243	0.917, 80	0.473, 39	0.304, 25	0.158, 13	0.049, 4	0.012, 1	
30%	0.364	1.214, 100	0.680, 56	0.425, 35	0.219, 18	0.061, 5	0.024, 2	
40%	0.486	1.214, 100	0.874, 72	0.546, 45	0.279, 23	0.085, 7	0.024, 2	

modified as a result of seeding by adding 1%–40% increases in IWC_B (from +0.012 to +0.486 g m⁻³) independent of the original background.

Figures 13i–l and Table 4 summarize the effects of seeding by modifying λ . From Table 4, for all wavelengths, an increase of 5 dB above background can be achieved if seeding produced an increase in IWC_B of at least 1% and background IWC was sufficiently low. The background IWC at W band to achieve a change in Z_e of 5 dB above background would have to be less than 0.02 IWC_B (0.024 g m⁻³) with a 1% seeding effect (+0.012 g m⁻³), less than 0.11 IWC_B (0.134 g m⁻³) with a 15% seeding effect (+0.182 g m⁻³), and less than 0.23 IWC_B (0.279 g m⁻³) with a 40% seeding effect (+0.486 g m⁻³). Notable wavelength differences appeared when λ was used to modify the distributions. The same change of 5 dB at Ka band with a 15% seeding effect (+0.182 g m⁻³) required an IWC < 0.24 IWC_B (0.291 g m⁻³), an IWC < 0.38 IWC_B (0.461 g m⁻³) at X band, and an IWC < 0.38 IWC_B (0.461 g m⁻³) at C band. In summary, adding large particles to the background particle size distributions by modifying λ resulted in larger increases in Z_e as a result of seeding, with a weaker constraint on background IWC in comparison with modifying n_o and μ .

In conclusion, regardless of how the size distributions were modified (i.e., decrease of n_o , μ , or λ), and regardless of the increase in IWC due to seeding (1%–40%; 0.012–0.486 g m⁻³), the change in Z_e for IWCs between 0.5 and 1.0 IWC_B (0.607 and 1.214 g m⁻³) was less than 5 dB.

5. Summary

This paper provides a quantitative analysis to assess if orographic cloud seeding effects are detectable using radar remote sensing when background precipitation is present. A gamma size distribution function was fit to a natural ice PSD representative of a heavily precipitating orographic cloud system from the SNOWIE field campaign. The value of the real part of the index of refraction (1.0316), appropriate for dry snow, was used so that the calculated Z_e assuming spherical particle shapes matched the measured Z_e from the Wyoming Cloud Radar at the University of Wyoming King Air, allowing us to retrieve the observed W-band reflectivity while also preserving the original size distribution. This gamma distribution was considered as the “baseline cloud IWC,” IWC_B = 1.214 g m⁻³. This distribution was then modified to

TABLE 4. As in Table 2, but background IWC was reduced by modifying λ .

% of IWC _B introduced by seeding	IWC introduced by seeding (g m ⁻³)	Background IWC (g m ⁻³), % of IWC _B (for different ΔZ_e)							
		1 dB	2 dB	3 dB	5 dB	10 dB	15 dB	20 dB	
W band									
1%	0.012	0.097, 8	0.061, 5	0.036, 3	0.024, 2	0.012, 1			
5%	0.061	0.291, 24	0.158, 13	0.109, 9	0.073, 6	0.024, 2	0.012, 1		
10%	0.121	0.510, 42	0.267, 22	0.182, 15	0.109, 9	0.049, 4	0.024, 2	0.012, 1	
15%	0.182	0.728, 60	0.364, 30	0.243, 20	0.134, 11	0.061, 5	0.024, 2	0.012, 1	
20%	0.243	0.947, 78	0.461, 38	0.304, 25	0.170, 14	0.073, 6	0.036, 3	0.012, 1	
30%	0.364	1.214, 100	0.656, 54	0.413, 34	0.231, 19	0.085, 7	0.036, 3	0.024, 2	
40%	0.486	1.214, 100	0.850, 70	0.534, 44	0.279, 23	0.097, 8	0.049, 4	0.024, 2	
Ka band									
1%	0.012	0.219, 18	0.158, 13	0.121, 10	0.085, 7	0.049, 4	0.024, 2	0.012, 1	
5%	0.061	0.473, 39	0.316, 26	0.255, 21	0.182, 15	0.097, 8	0.061, 5	0.036, 3	
10%	0.121	0.680, 56	0.449, 37	0.340, 28	0.243, 20	0.134, 11	0.073, 6	0.049, 4	
15%	0.182	0.862, 71	0.546, 45	0.413, 34	0.291, 24	0.158, 13	0.097, 8	0.061, 5	
20%	0.243	1.032, 85	0.643, 53	0.486, 40	0.328, 27	0.170, 14	0.109, 9	0.061, 5	
30%	0.364	1.214, 100	0.801, 66	0.595, 49	0.401, 33	0.206, 17	0.121, 10	0.073, 6	
40%	0.486	1.214, 100	0.947, 78	0.704, 58	0.461, 38	0.231, 19	0.134, 11	0.085, 7	
X band									
1%	0.012	0.376, 31	0.279, 23	0.231, 19	0.170, 14	0.109, 9	0.061, 5	0.036, 3	
5%	0.061	0.668, 55	0.498, 41	0.413, 34	0.316, 26	0.182, 15	0.121, 10	0.073, 6	
10%	0.121	0.850, 70	0.631, 52	0.522, 43	0.401, 33	0.243, 20	0.158, 13	0.097, 8	
15%	0.182	0.983, 81	0.741, 61	0.607, 50	0.461, 38	0.279, 23	0.182, 15	0.121, 10	
20%	0.243	1.093, 90	0.813, 67	0.668, 55	0.510, 42	0.304, 25	0.194, 16	0.134, 11	
30%	0.364	1.214, 100	0.947, 78	0.777, 64	0.595, 49	0.352, 29	0.231, 19	0.146, 12	
40%	0.486	1.214, 100	1.044, 86	0.862, 71	0.656, 54	0.388, 32	0.255, 21	0.170, 14	
C band									
1%	0.012	0.388, 32	0.291, 24	0.243, 20	0.182, 15	0.109, 9	0.073, 6	0.049, 4	
5%	0.061	0.608, 56	0.510, 42	0.425, 35	0.328, 27	0.194, 16	0.121, 10	0.085, 7	
10%	0.121	0.862, 71	0.656, 54	0.546, 45	0.413, 34	0.255, 21	0.158, 13	0.109, 9	
15%	0.182	0.983, 81	0.741, 61	0.607, 50	0.461, 38	0.279, 23	0.182, 15	0.121, 10	
20%	0.243	1.105, 91	0.826, 68	0.692, 57	0.522, 43	0.316, 26	0.206, 17	0.134, 11	
30%	0.364	1.214, 100	0.959, 79	0.801, 66	0.607, 50	0.364, 30	0.243, 20	0.158, 13	
40%	0.486	1.214, 100	1.056, 87	0.874, 72	0.668, 55	0.413, 34	0.267, 22	0.182, 15	

create 297 artificial background size distributions with lower IWC to simulate lighter precipitation events to determine when seeding would be detectable in these events using radar. The effects of seeding were carried out by adding to these distributions a Δ of IWC_B ranging from 1% to 40%. Changes in Z_e due to seeding relative to the background distributions prior to seeding were then calculated for all 297 background and seeded distributions for three cases: modifying n_o while holding λ and μ constant, modifying μ while holding n_o and λ constant, and modifying λ while holding n_o and μ constant.

Figure 13 showed that each seeded IWC curve has an inflection point in which the background IWC is sufficiently small that the change in Z_e as a result of seeding begins to increase to the point of detectability (e.g., ≥ 5 dB). The results, taken in sum, show that to have an increase in Z_e that is distinguishable from the background, the seeding effect must be large and the background IWC must be very small relative to the IWC measured during the heavy background precipitating event during SNOWIE.

The implication of these results is that when background precipitation is present seeding effects cannot be detected, so

it remains uncertain whether seeding had no effect on cloud microstructure and therefore produced no signature on radar, or whether seeding did have an effect but that effect was undetectable against the background reflectivity associated with naturally produced precipitation.

We note that, to make the calculations tractable, our approach to calculate the radar reflectivity used the assumption that the particles had spherical shapes, an index of refraction consistent with dry snow, and with density following the Brown and Francis (1995). A more sophisticated approach would be to assume a habit distribution and perform more complex scattering calculations that would refine these results. However, we believe that the fundamental conclusions would remain the same. That is, it will be difficult to directly observe changes in cloud reflectivity structure associated with seeding in heavily precipitating orographic clouds using ground-based and airborne radars.

In future field campaigns, efforts should therefore be made to include alternate methodologies to determine the efficacy of orographic cloud seeding when heavy background precipitation is present. Examples include analysis of anomalous

concentrations of silver in snow (e.g., Fisher et al. 2016, 2018) or the ratio of silver to a nonnucleating, naturally covarying aerosol tracer such as indium oxide (Warburton et al. 1995; Manton and Warren 2011), as well as airborne observations of the microphysical chain of events associated with seeding from initiation to the growth of ice crystals to precipitation. Models also provide yet another approach to evaluate the physical chain of events associated with seeding and the impact on orographic precipitation (e.g., Xue et al. 2022).

Acknowledgments. We thank the crews from the University of Wyoming King Air (UWKA) and the Doppler on Wheels radars, as well as all principal investigators and students from the Universities of Colorado, Wyoming, and Illinois and the National Center for Atmospheric Research, and we thank Idaho Power Company for their help in operating and deploying instruments during the campaign and providing comments on this research. We also thank Dr. Jeffrey French and Adam Majewski for processing and creating the UWKA particle size distribution dataset. We particularly thank the reviewers of this paper for their careful comments, which resulted in a much more thorough and complete analysis. Funding for the UWKA and WCR during SNOWIE was provided through the National Science Foundation (NSF) Award AGS-1441831. This research was supported under NSF AGS-1546939, and AGS-2016106, and the Cooperative Institute for Severe and High Impact Weather Research and Operations (CIWRO).

Data availability statement. All data presented here are publicly available through the SNOWIE data archive website (https://data.eol.ucar.edu/master_lists/generated/snowie/) maintained by the Earth Observing Laboratory at the National Center for Atmospheric Research.

REFERENCES

- Atlas, D., S. Y. Matrosov, A. J. Heymsfield, M.-D. Chou, and D. B. Wolff, 1995: Radar and radiation properties of ice clouds. *J. Appl. Meteor.*, **34**, 2329–2345, [https://doi.org/10.1175/1520-0450\(1995\)034<2329:RARPOI>2.0.CO;2](https://doi.org/10.1175/1520-0450(1995)034<2329:RARPOI>2.0.CO;2).
- Baumgardner, D., and Coauthors, 2017: Cloud ice properties: In situ measurement challenges. *Ice Formation and Evolution in Clouds and Precipitation: Measurement and Modeling Challenges*, Meteor. Monogr., No. 58, Amer. Meteor. Soc., <https://doi.org/10.1175/AMSMONOGRAPHS-D-16-0011.1>.
- Brown, P. R. A., and P. N. Francis, 1995: Improved measurements of the ice water content in cirrus using a total-water probe. *J. Atmos. Oceanic Technol.*, **12**, 410–414, [https://doi.org/10.1175/1520-0426\(1995\)012<0410:IMOTIW>2.0.CO;2](https://doi.org/10.1175/1520-0426(1995)012<0410:IMOTIW>2.0.CO;2).
- Deng, M., J. French, B. Geerts, S. Haimov, L. Oolman, D. Plummer, and Z. Wang, 2022: Retrieval and evaluation of ice water content from the airborne Wyoming Cloud Radar in orographic wintertime clouds during SNOWIE. *J. Atmos. Oceanic Technol.*, **39**, 207–221, <https://doi.org/10.1175/JTECH-D-21-0085.1>.
- Deshler, T., D. W. Reynolds, and A. W. Huggins, 1990: Physical response of winter orographic clouds over the Sierra Nevada to airborne seeding using dry ice or silver iodide. *J. Appl. Meteor.*, **29**, 288–330, [https://doi.org/10.1175/1520-0450\(1990\)029<0288:PROWOC>2.0.CO;2](https://doi.org/10.1175/1520-0450(1990)029<0288:PROWOC>2.0.CO;2).
- Eriksson, P., R. Ekelund, J. Mendrok, M. Brath, O. Lemke, and S. A. Buehler, 2018: A general database of hydrometeor single scattering properties at microwave and sub-millimetre wavelengths. *Earth Syst. Sci. Data*, **10**, 1301–1326, <https://doi.org/10.5194/essd-10-1301-2018>.
- Evans, K. F., 1998: The spherical harmonics discrete ordinate method for three-dimensional atmospheric radiative transfer. *J. Atmos. Sci.*, **55**, 429–446, [https://doi.org/10.1175/1520-0469\(1998\)055<0429:TSHDOM>2.0.CO;2](https://doi.org/10.1175/1520-0469(1998)055<0429:TSHDOM>2.0.CO;2).
- Faber, S., 2017: Error Characterization for airborne probes using laboratory calibration and in-situ analysis. M.S. thesis, Dept. of Atmospheric Science, University of Wyoming, 102 pp., https://www.uwyo.edu/atsc/directory/faculty/French/french-research/class_materials/faber_thesis_final.pdf.
- Fisher, J. M., M. L. Lytle, M. L. Kunkel, D. Blestrud, V. P. Holbrook, S. K. Parkinson, P. R. Edwards, and S. G. Benner, 2016: Evaluation of glaciogenic cloud seeding using trace chemistry. *J. Wea. Modif.*, **48**, 24–42, <https://doi.org/10.54782/jwm.v48i1.548>.
- , —, —, D. R. Blestrud, N. W. Dawson, S. K. Parkinson, R. Edwards, and S. G. Benner, 2018: Assessment of ground-based and aerial cloud seeding using trace chemistry. *Adv. Meteor.*, **2018**, 7293987, <https://doi.org/10.1155/2018/7293987>.
- Flossmann, A. I., M. Manton, A. Abshaev, R. Brientjes, M. Murakami, T. Prabhakaran, and Z. Yao, 2019: Review of advances in precipitation enhancement research. *Bull. Amer. Meteor. Soc.*, **100**, 1465–1480, <https://doi.org/10.1175/BAMS-D-18-0160.1>.
- French, J. R., and Coauthors, 2018: Precipitation formation from orographic cloud seeding. *Proc. Natl. Acad. Sci. USA*, **115**, 1168–1173, <https://doi.org/10.1073/pnas.1716995115>.
- Friedrich, K., and Coauthors, 2020: Quantifying snowfall from orographic cloud seeding. *Proc. Natl. Acad. Sci. USA*, **117**, 5190–5195, <https://doi.org/10.1073/pnas.1917204117>.
- , and Coauthors, 2021: Microphysical characteristics and evolution of seeded orographic clouds. *J. Appl. Meteor. Climatol.*, **60**, 909–934, <https://doi.org/10.1175/JAMC-D-20-0206.1>.
- Geerts, B., and Coauthors, 2013: The AgI Seeding Cloud Impact Investigation (ASCI) campaign 2012: Overview and preliminary results. *J. Wea. Modif.*, **45**, 24–43, <https://doi.org/10.54782/jwm.v45i1.121>.
- Heggli, M. F., and R. M. Rauber, 1988: The characteristics and evolution of supercooled water in wintertime storms over the Sierra Nevada: A summary of microwave radiometric measurements taken during the Sierra Cooperative Pilot Project. *J. Appl. Meteor.*, **27**, 989–1015, [https://doi.org/10.1175/1520-0450\(1988\)027<0989:TCAEOS>2.0.CO;2](https://doi.org/10.1175/1520-0450(1988)027<0989:TCAEOS>2.0.CO;2).
- Heimes, K., and Coauthors, 2022: Vertical motions in orographic cloud systems over the Payette River basin. Part III: An evaluation of the impact of transient vertical motions on targeting during orographic cloud seeding operations. *J. Appl. Meteor. Climatol.*, **61**, 1753–1777, <https://doi.org/10.1175/JAMC-D-21-0230.1>.
- Hobbs, P. V., J. H. Lyons, J. D. Locatelli, K. R. Biswas, L. F. Radke, R. R. Weiss Sr., and A. L. Rangno, 1981: Radar detection of cloud-seeding effects. *Science*, **213**, 1250–1252, <https://doi.org/10.1126/science.213.4513.1250>.
- Hong, G., P. Yang, B. A. Baum, and A. J. Heymsfield, 2008: Relationship between ice water content and equivalent radar reflectivity for clouds consisting of nonspherical ice

- particles. *J. Geophys. Res.*, **113**, D20205, <https://doi.org/10.1029/2008JD009890>.
- Jackson, R. C., G. M. McFarquhar, J. Stith, M. Beals, R. A. Shaw, J. Jensen, H. Fugal, and A. Korolev, 2014: An assessment of the impact of antishattering tips and artifact removal techniques on cloud ice size distributions measured by the 2D cloud probe. *J. Atmos. Oceanic Technol.*, **31**, 2567–2590, <https://doi.org/10.1175/JTECH-D-13-00239.1>.
- Knollenberg, R. G., 1981: Techniques for probing cloud microstructure. *Clouds, Their Formation, Optical Properties and Effects*, P. V. Hobbs and A. Deepak, Eds., Academic Press, 15–89, <https://doi.org/10.1016/B978-0-12-350720-4.X5001-7>.
- Korolev, A. V., J. W. Strapp, G. A. Isaac, and A. N. Nevzorov, 1998: The Nevzorov airborne hot-wire LWC–TWC probe: Principle of operation and performance characteristics. *J. Atmos. Oceanic Technol.*, **15**, 1495–1510, [https://doi.org/10.1175/1520-0426\(1998\)015<1495:TNAHWL>2.0.CO;2](https://doi.org/10.1175/1520-0426(1998)015<1495:TNAHWL>2.0.CO;2).
- , —, —, and E. Emery, 2013: Improved airborne hot-wire measurements of ice water content in clouds. *J. Atmos. Oceanic Technol.*, **30**, 2121–2131, <https://doi.org/10.1175/JTECH-D-13-00007.1>.
- Lawson, R. P., D. O'Connor, P. Zmarzly, K. Weaver, B. A. Baker, Q. Mo, and H. Jonsson, 2006: The 2DS (stereo) probe: Design and preliminary tests of a new airborne, high-speed, high-resolution particle imaging probe. *J. Atmos. Oceanic Technol.*, **23**, 1462–1477, <https://doi.org/10.1175/JTECH1927.1>.
- Manton, M. J., and L. Warren, 2011: A confirmatory snowfall enhancement project in the snowy mountains of Australia. Part II: Primary and associated analyses. *J. Appl. Meteor. Climatol.*, **50**, 1448–1458, <https://doi.org/10.1175/2011JAMC2660.1>.
- McFarquhar, G. M., T.-L. Hsieh, M. Freer, J. Mascio, and B. F. Jewett, 2015: The characterization of ice hydrometeor gamma size distributions as volumes in N_{σ} – λ – μ phase space: Implications for microphysical process modeling. *J. Atmos. Sci.*, **72**, 892–909, <https://doi.org/10.1175/JAS-D-14-0011.1>.
- , J. A. Finlon, D. M. Stechman, W. Wu, R. C. Jackson, and M. Freer, 2018: University of Illinois/Oklahoma Optical Array Probe (OAP) Processing Software, version v3.1.4. Zenodo, <https://zenodo.org/records/1285969>.
- Pazmany, A. L., R. E. McIntosh, R. D. Kelly, and G. Vali, 1994: An airborne 95 GHz dual-polarized radar for cloud studies. *IEEE Trans. Geosci. Remote Sens.*, **32**, 731–739, <https://doi.org/10.1109/36.298002>.
- Pokharel, B., B. Geerts, and X. Jing, 2014: The impact of ground-based glaciogenic seeding on orographic clouds and precipitation: A multisensor case study. *J. Appl. Meteor. Climatol.*, **53**, 890–909, <https://doi.org/10.1175/JAMC-D-13-0290.1>.
- Protat, A., and Coauthors, 2016: The measured relationship between ice water content and cloud radar reflectivity in tropical convective clouds. *J. Appl. Meteor. Climatol.*, **55**, 1707–1729, <https://doi.org/10.1175/JAMC-D-15-0248.1>.
- Rasmussen, R. M., and Coauthors, 2018: Evaluation of the Wyoming Weather Modification Pilot Project (WWMPP) using two approaches: Traditional statistics and ensemble modeling. *J. Appl. Meteor. Climatol.*, **57**, 2639–2660, <https://doi.org/10.1175/JAMC-D-17-0335.1>.
- Rauber, R. M., and L. O. Grant, 1986: The characteristics and distribution of cloud water over the mountains of northern Colorado during wintertime storms. Part II: Spatial distribution and microphysical characteristics. *J. Climate Appl. Meteor.*, **25**, 489–504, [https://doi.org/10.1175/1520-0450\(1986\)025<0489:TCADOC>2.0.CO;2](https://doi.org/10.1175/1520-0450(1986)025<0489:TCADOC>2.0.CO;2).
- , and S. W. Nesbitt, 2018: *Radar Meteorology: A First Course*. Wiley, Inc., 496 pp.
- , and Coauthors, 2019: Wintertime orographic cloud seeding—A review. *J. Appl. Meteor. Climatol.*, **58**, 2117–2140, <https://doi.org/10.1175/JAMC-D-18-0341.1>.
- Reynolds, D. W., and A. S. Dennis, 1986: A review of the Sierra Cooperative Pilot Project. *Bull. Amer. Meteor. Soc.*, **67**, 513–523, [https://doi.org/10.1175/1520-0477\(1986\)067<0513:AROTSC>2.0.CO;2](https://doi.org/10.1175/1520-0477(1986)067<0513:AROTSC>2.0.CO;2).
- Sadiku, M. N. O., 1985: Refractive index of snow at microwave frequencies. *Appl. Opt.*, **24**, 572–575, <https://doi.org/10.1364/AO.24.000572>.
- Strapp, J. W., L. E. Lilie, E. Emery, and D. Miller, 2005: Preliminary comparison of ice water content as measured by hot wire instruments of varying configuration. Preprints, *43rd AIAA Aerospace Sciences Meeting and Exhibit*, Reno, NV, AIAA, AIAA 2005-0860, <https://doi.org/10.2514/6.2005-860>.
- Tessendorf, S. A., and Coauthors, 2019: Transformational approach to winter orographic weather modification research: The SNOWIE project. *Bull. Amer. Meteor. Soc.*, **100**, 71–92, <https://doi.org/10.1175/BAMS-D-17-0152.1>.
- Wang, J., Z. Yue, D. Rosenfeld, L. Zhang, Y. Zhu, J. Dai, X. Yu, and J. Li, 2021: The evolution of an AgI cloud-seeding track in central China as seen by a combination of radar, satellite, and disdrometer observations. *J. Geophys. Res. Atmos.*, **126**, e2020JD033914, <https://doi.org/10.1029/2020JD033914>.
- Wang, Z., and Coauthors, 2012: Single aircraft integration of remote sensing and in situ sampling for the study of cloud microphysics and dynamics. *Bull. Amer. Meteor. Soc.*, **93**, 653–668, <https://doi.org/10.1175/BAMS-D-11-00044.1>.
- Warburton, J. A., L. G. Young, and R. H. Stone, 1995: Assessment of seeding effects in snowpack augmentation programs: Ice nucleation and scavenging of seeding aerosols. *J. Appl. Meteor.*, **34**, 121–130, <https://doi.org/10.1175/1520-0450-34.1.121>.
- Wurman, J., and Coauthors, 2021: The Flexible Array of Radars and Mesonets (FARM). *Bull. Amer. Meteor. Soc.*, **102**, E1499–E1525, <https://doi.org/10.1175/BAMS-D-20-0285.1>.
- Xue, L., and Coauthors, 2022: Comparison between observed and simulated AgI seeding impacts in a well-observed case from the SNOWIE field program. *J. Appl. Meteor. Climatol.*, **61**, 345–367, <https://doi.org/10.1175/JAMC-D-21-0103.1>.
- Zaremba, T. J., and Coauthors, 2022: Vertical motions in orographic cloud systems over the Payette River basin. Part II: Fixed and transient updrafts and their relationship to forcing. *J. Appl. Meteor. Climatol.*, **61**, 1733–1751, <https://doi.org/10.1175/JAMC-D-21-0229.1>.